Research papers

Binderless synthesis of hierarchical, marigold flower-like NiCo$_2$O$_4$ films for high-performance symmetric supercapacitor

P.S. Naik [a], R.S. Redekar [b], Jayashri V. Kamble [c], K.V. Patil [b], S.N. Tayade [c], V.L. Patil [d], N.L. Tarwal [b,*], M.M. Karanjakar [e,*], P.D. Kamble [f,*]

[a] Department of Physics, Prof. Dr. N. D. Patil Mahavidyalaya, Malkapur, M.S. 415 101, India
[b] Smart Materials Research Laboratory, Shivaji University, Kolhapur, M.S. 416 004, India
[c] Department of Chemistry, Shivaji University, Kolhapur, M.S. 416 004, India
[d] Thin Films Materials Laboratory, Shivaji University, Kolhapur, M.S. 416 004, India
[e] Department of Physics, Vivekanand College, Kolhapur, M.S. 415 101, India
[f] Department of Physics, The New College, Kolhapur, M.S. 415 101, India

ARTICLE INFO

ABSTRACT

The facile and cost-effective chemical bath deposition method is employed for the binder-free synthesis of NiCo$_2$O$_4$ marigold flower-like nanostructures on a flexible stainless-steel substrate. Binderless and surfactant-free synthesis of NiCo$_2$O$_4$ films for supercapacitor application is a crucial part of this synthesis process. The effect of reaction times on the deposition of NiCo$_2$O$_4$ nanostructured films has been discussed briefly based on the electrochemical performance and surface morphology of films. The reaction time is varied as 2, 4, 6, and 8 h. The prepared films were analyzed by structural and morphological characterizations. The time-dependent significant change in morphology of NiCo$_2$O$_4$ films is discussed in detail. The development of the Marigold-like flowers from wheat grain-like nanostructures has been observed for increasing reaction time. The film deposited at 6 h reaction time (NCO-6 electrode) showed better specific capacitance of 1277 F/g at 5 mA/cm^2, which retained about 95 % after 10,000 cycles. The NiCo$_2$O$_4$ film exhibited a 0.7 V potential window with the maximum energy and power density of 86 Wh/kg and 2333 W/kg, respectively. The fabricated aqueous symmetric device i.e., NCO//NCO showed energy density and power density of 16.4 Wh/kg and 275.5 W/kg, respectively. The fabricated device shows 90.5 % retention in performance after 5000 cycles. These results revealed that NiCo$_2$O$_4$ can be a better electrode material for energy storage devices.

1. Introduction

Today, much of our energy consumption relies on renewable sources, driven by climate change concerns and the finite nature of fossil fuels. Consequently, the global community has increasingly turned to solar and wind power, aiming to minimize carbon dioxide emissions through the adoption of electric and hybrid vehicles. Nowadays, the use of green energy sources like solar, wind, hydro, tidal, geothermal, bio-energies, nanogenerators etc. is increasing tremendously. Nevertheless, the intermittent nature of these sources necessitates efficient energy storage solutions when the primary source is unavailable. To address this challenge, supercapacitors and batteries have emerged as vital mechanisms for energy storage [1–3]. Supercapacitors are being well popularized due to their low cost, high performance, and quick charge-

discharge behavior [4]. Also, it shows more reliability, high power density, high charge transfer ability, and good cyclic stability ~10^5 cycles [5]. The carbon-containing materials like active and porous carbon, graphene, and carbon nanotubes exhibit high power density, low specific capacitance, and low energy density restricting their use in high-energy circuits. In this regard, the researchers are focused on the faradaic electrode materials with increased capacity and energy density. In recent years, metal oxides, hydroxides, sulfides, and conducting polymers have been enormously used in energy storage devices [6,7]. MnO$_2$ [8], MOFs [9], and Co$_3$O$_4$ [10] are the most well-known faradaic electrode materials with low intrinsic electrical conductivity. Recently, mixed transition metal oxides (MTMOs) have garnered significant attention in energy-related applications. The inclusion of multiple metal species in MTMOs has proven beneficial in enhancing redox reactions

---

* Corresponding authors.
E-mail addresses: nlt.phy@unishivaji.ac.in (N.L. Tarwal), ncrtnt2012@gmail.com (M.M. Karanjakar), pdkamble27@gmail.com (P.D. Kamble).

within electrolyte solutions, while also providing a high electrical conductivity advantageous for electrochemical applications [11]. Nickel cobaltite (NiCo$_2$O$_4$ or NCO) is a low-cost, less toxic, highly elemental abundant, and has a diverse morphological appearance which is feasible to get superior electrochemical properties [12]. NiCo$_2$O$_4$ can provide richer redox chemistry and integrate the contributions from both nickel and cobalt ions in comparison to the two single component oxides i.e. nickel oxide, and cobalt oxide [13]. NiCo$_2$O$_4$ has at least two orders of magnitude better electrical conductivity than monometallic nickel and cobalt oxides because of the existence of mixed valences of the same cation in such spinel cobaltite [14]. This is because electrons are transported between cations with comparatively low activation energy [15]. The ternary materials have a substantially greater electrical conductivity than the binary electrode materials, which helps the electrode to perform significantly better in terms of storage, particularly concerning its high rate capabilities [16]. The various crystal structures and rational morphological designs are concerned with improving the electrochemical performance of electrode materials. Till now, NCO nanostructures like nanofibers, nanoneedles, nanorods, nanowires, nanosheets, nanospheres, nanoflowers, etc. were synthesized by hydrothermal [17], solvothermal [18], screen printing [19], electrodeposition [20], and spray pyrolysis method [21]. Some of these methods are and multistep which require more time for device fabrication which increases cost. Among them, Chemical bath deposition (CBD) is a well-known chemical method used for the morphology-controlled synthesis of material by varying time, temperature, pH, solvent, solute concentration, etc. Therefore, we have used the CBD method for the synthesis of NCO nanostructures. In a charge storage mechanism, the highly porous material plays a wide role in the enhancement of surface area and active sites on the material surface. Oftenly, polymer binders are used to coat a thin film on the substrate surface but they reduce active sites and electrochemical performance of material. Therefore, binder-free electrode deposition is essential for improving the supercapacitive behavior of the material. As a result, researchers are eager to develop binder-free thin film.

Till now, very few reports are available on the binder-free synthesis of the NCO nanostructure on stainless steel (SS) substrate by chemical methods. Recently, Salunkhe et al. [22] have synthesized the NCO nanorods by the CBD method which showed a 490 F/g specific capacitance (C$_{sp}$) at 2 mV/s with an energy density of 45 Wh/kg and power densities of 2 kW/kg, respectively. The fabricated device showed 97 % stability after 1000 charge-discharge cycles. Meanwhile, Waghmode et al. [23] have synthesized NCO nanoflower by the CBD method with a C$_{sp}$ of 540 F/g at 5 mV/s, in which the electrode showed 93.5 % retention in cyclic stability after 1000 charge-discharge cycles. The fabricated NCO electrode revealed the energy and power density of 56 Wh/kg and 5.7 kW/kg, respectively. Moreover, Dhavale et al. [5] have grown the NCO thin film on SS substrate by a simple CBD method. The reaction was carried out by using different solvents which led to the formation of different NCO nanostructure formation. The binder-less synthesis of NCO thin film with a high C$_{sp}$ of 553 F/g at 0.5 mA/cm^2 exhibited 90 % cycling stability after 2000 cycles. Binder-free synthesis in the CBD method provided an excellent path to grow NCO thin films with highly uniform porous structures that can deliver a high supercapacitive performance. Similarly, Kamble et al. [24] synthesized porous marigold micro-flower-like NCO by CBD method, in which a fabricated device showed a 530 F/g at 6 mA/cm^2 with stability of 90.5 % retention after 3000 cycles. These studies highlighted the benefits of binder-less synthesis of the NCO nanostructure and motivated enhancement in the electrochemical performance using simple and cost-effective CBD methods. Nevertheless, the study on the binder-less synthesis of NCO offers improved charge storage; however, performance enhancement can still be achieved with the aid of novel morphologies. As mentioned earlier, the CBD method can yield hierarchical morphologies and improved performance. Motivated by this, we synthesized marigold flower-like NCO structures on a flexible stainless steel substrate by varying the reaction time, a novel approach that has not yet been studied.

Herewith, we have reported the binder-less growth of marigold flower-like NCO structures on flexible SS substrate using the CBD method for supercapacitor application. The growth of the NCO nanostructure has been optimized by varying the reaction time. The deposited NCO films exhibited a growth transformation from wheat grain-like to marigold flower-like structures with increasing reaction time. The NCO film deposited at 6 h reaction time showed the formation of a highly porous marigold flower-like structure which is advantageous for energy storage mechanism in aqueous alkali electrolytes. However, a symmetric supercapacitor device based on the marigold flower-like NCO film has been tested to check the real-time applicability of the material. Based on the obtained results and device performance, marigold flower-like NCO films can be used as an attractive and promising electrode material.

2. Experimental

2.1. Materials

Nickel nitrate hexahydrate (Ni(NO$_3$)$_2$.6H$_2$O), Cobalt nitrate hexahydrate (Co(NO$_3$)$_2$.6H$_2$O), Urea (CO(NH$_2$)$_2$), and Ammonium fluoride (NH$_4$F) were purchased from Sigma Aldrich and used without further purification. The stainless steel (SS) substrates were purchased from Micromesh India Pvt. Ltd. and double distilled water (DDW) was used for the solution preparation.

2.2. Synthesis of NiCo$_2$O$_4$ films by a chemical bath deposition method

In this study, nanostructured NiCo$_2$O$_4$ films were prepared using the chemical bath deposition method. A piece of SS (3 cm × 1 cm) was ultrasonically washed with a soap solution, and water and then polished with zero-grade polish paper. In 50 ml DDW, Ni(NO$_3$)$_2$.6H$_2$O (0.05 M), Co(NO$_3$)$_2$.6H$_2$O (0.1 M), (CO(NH$_2$)$_2$) (0.3 M), and NH$_4$F (0.2 M) were taken and stirred for 1 h. In a CBD method, 50 ml beaker containing precursors solution was put in a hot water bath with a temperature of 90 °C. Later on, the flexible SS substrates were vertically immersed in the solution for 2 h. A film of NiCo-hydroxide was formed as a result of the chemical precipitation reaction. After the reaction, pink-colored, and homogeneous NCO films were deposited. Later it was taken out and washed several times with DDW and ethanol for removal of loose particles. After that, the NCO films were put into the oven for drying at 70 °C for 8 h. Finally, the NCO nanostructured films were annealed at 350 °C for 3 h to avoid the thermal corrosion of stainless steel as well as to obtain the NiCo$_2$O$_4$ phase [5]. A similar deposition procedure was carried out by varying the reaction times to 4, 6, and 8 h and the NCO films were named NCO-2, NCO-4, NCO-6, and NCO-8, respectively. The schematic representation of the synthesis process is shown in the Fig. 1.

2.3. Characterization techniques

A crystallographic characterization was recorded using a Bruker D8 Advanced X-ray diffractometer (XRD, Cu K$_\alpha$-1.54 Å) for structural identification. The surface analysis was carried out by Scanning electron microscopy (SEM; JEOL-JSM6360). The functional group present in the material was studied by Fourier transform infrared spectroscopy (JASCO FTIR 4700) technique in the range of 4000–400 cm^{-1}. The phases present in the material were analyzed by FT-Raman spectroscopy (Bruker Germany, multi-RAM, Nd-YAG) to study the Raman active bonds. Surface chemical configuration was determined by X-ray photoelectron spectroscopy (XPS; Thermo Scientific, UK). Transmission electron microscopy with high resolution (HRTEM; Tecnai F21) was used to examine surface morphology. The surface area, pore size, and pore volume distribution of the NCO powder sample were studied by Brunauer-Emmett-Teller (BET, Quantachrome NOVA 1000e, USA).
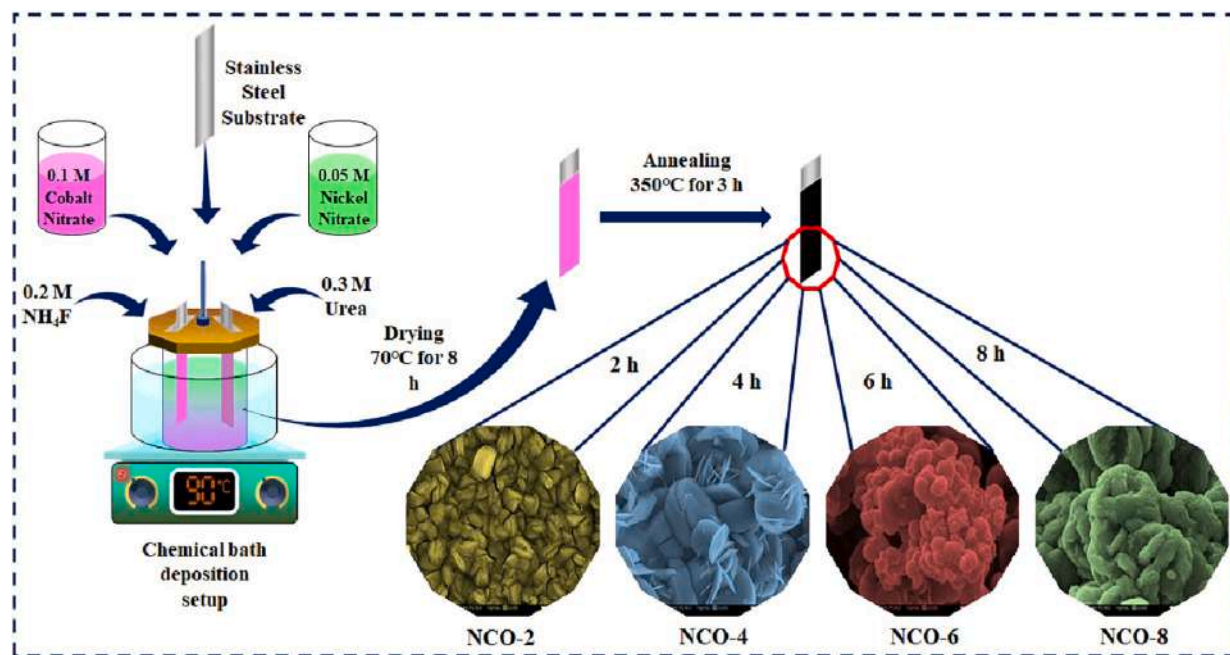
Fig. 1. Schematic representation of the synthesis of NiCo$_2$O$_4$ films by varying different reaction time.

2.4. Electrochemical measurement

The electrochemical analysis of NCO nanostructured films was performed by potentiostat Autolab (PGSTAT302N). The electrochemical performance of all NCO films was studied with saturated calomel electrode (SCE) as a reference, graphite electrode as a counter, and NCO films as a working electrode immersed in an electrolyte solution. The cyclic voltammetry (CV) tests were performed by scan rates from 5 to 100 mV/s in a potential range of −0.3 to +0.5 V (vs. SCE), whereas, the galvanostatic charge-discharge (GCD) analysis was carried out at 5 to 25 mA/cm^2 current densities. Electrochemical impedance spectroscopy (EIS) was performed in the 0.1 to 10^5 Hz frequency range. The following formulae were used to find out the C_{sp} of NCO films from GCD curves,

$$C_{sp} = \frac{I \times \Delta t}{m \times \Delta V} \tag{1}$$

where, I is a current density (mA/cm^2), Δt is discharge time (s), m is an active mass (g), and ΔV is a potential window (V).

The specific energy density E (Wh/Kg) and power density P (W/Kg) were calculated from the discharge curve using the following formulas,

$$E = \frac{C_{sp} \times \Delta V^2}{2 \times 3.6} \tag{2}$$

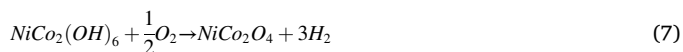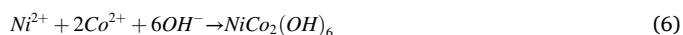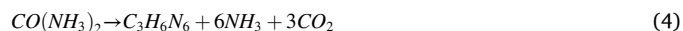$$P = \frac{E \times 3600}{\Delta t} \tag{3}$$

3. Results and discussion

3.1. NiCo$_2$O$_4$ film growth mechanism

In the CBD process, the addition of urea results in ammonium hydroxide production, and its breakdown into ammonia, raising the pH of the solution with mixed hydroxides of Ni and Co metal ions [25]. The electrostatic and Van der Waals forces led to attracting hydrolyzed metal ions. The bath solution temperature of 90 °C allowed to creation of the nucleation centers of metal hydroxide ions on the substrate by providing sufficient energy. The deposition medium contained the Ni^{2+} and Co^{2+} metal salts with urea as a complexing agent [26]. In this process, the NH$_4$F is used for surface co-modification which creates F$^-$ ions when

dissolved in water. This facilitated more nucleation sites on the SS substrate surface in aqueous medium [27].

The nickel-cobalt hydroxide formation process is as given in Eqs. (4) to (6);

$$CO(NH_3)_2 \rightarrow C_3H_6N_6 + 6NH_3 + 3CO_2 \tag{4}$$

$$NH_3 + H_2O \rightarrow NH_4^+ + OH^- \tag{5}$$

$$Ni^{2+} + 2Co^{2+} + 6OH^- \rightarrow NiCo_2(OH)_6 \tag{6}$$

$$NiCo_2(OH)_6 + \frac{1}{2}O_2 \rightarrow NiCo_2O_4 + 3H_2 \tag{7}$$

The annealing at higher temperatures is used to change the hydroxide into the oxide phase (NiCo$_2$O$_4$) [28]. After 3 h of annealing at 350 °C, the Ni—Co hydroxides released water molecules and shaped from wheat grain to marigold flower-like NCO-nanostructures on the SS-substrate [29]. The diffusion and nucleation rates were highly dependent on the reaction times of nanostructured NCO resulting in the formation of various morphologies due to offering different rates for chemical reaction. As a consequence, the crystals grew in 2D or 3D morphologies. The particle nucleation, aggregation, and coalescence are the three major steps for the NCO-nanostructure formation [30]. The shape evolution process involves the generation of nucleation centers that attract more cations towards the substrate to form nanoparticles. The wheat grain-like morphology of NCO film was observed at a reaction time of 2 h. As reaction time increased from 4 to 6 h, the nanoplates aggregated to form a marigold nanoflower-like structure of NCO with a high surface-to-volume ratio, whereas, the reaction time exceeding 8 h led to overgrowth formation on the film surface [31]. A similar morphology transformation was reported by Kamble et al. [24]. The synthesized NCO with marigold flower-like morphology on SS-mesh substrate by simple CBD method offered a large surface area of 100.27 m^2/g and resulted in a high specific capacitance of 530 F/g at 6 mA/cm^2.

3.2. Structural analysis

The XRD analysis is used to study the material structural analysis of

nanostructured NCO films. The XRD patterns of NCO nanostructured films deposited by varying reaction time from 2 to 8 h with annealing at 350 °C are shown in Fig. 2(a). The diffraction peaks occurred at 2θ angles of 18.92°, 31.15°, 36.07°, 43.59°, and 64.09°, representing (111), (220), (311), (400), and (440) lattice planes, respectively. The XRD patterns revealed that deposited material is polycrystalline which is well-matched with the standard data card (ICDD card no. 00-073-1702) [32]. The diffraction peaks well agreed with the cubic spinel crystal structure (Fd-3m) and * indicates the peaks due to the SS substrate. The Debye Scherrer formula was used to calculate the crystallite size for the most intense peak (311) as shown in Eq. (8) [33].

$$D = \frac{K\lambda}{\beta \cos\theta} \tag{8}$$

where, the crystallite size (D), shape factor (K), the wavelength of monochromatic X-ray (λ = 1.5418 Å), full width at half maxima of the peak (β), and diffraction angle (θ) [34].

By comparing all samples, the peak intensity of the (311) plane for the NCO-2 sample showed high crystallinity and a more intense peak. The crystallite sizes of NCO film samples were observed as 45.6, 39.87, 27.98, and 30.56 nm for NCO-2, NCO-4, NCO-6, and NCO-8 samples, respectively, which were decreased with reaction time. The lower crystallite size could be due to the deposition of the less crystalline grain

on the surface of the substrate as the reaction time increased. For the NCO-6 film, the crystallite size was smaller than others. Such a smaller crystallite size can offer more flexible bonding and resulted in pseudo-capacitive charge storage. The lattice parameters of all the samples were found to be a = b = c = 8.114 Å [35]. The charge storage capability of the material is due to the instant ion diffusion in the material because of the nanosized nature of NCO. Also, the size reduction in the crystallite size increased the chances of the intercalation of the electrolyte ions in the NCO films [36].

The FT-IR spectra of NCO films were recorded to confirm the presence of functional groups in the material. From Fig. 2(b), the metal oxide (M-O) peaks observed at 557 and 648 cm^{-1} correspond to the vibrational frequencies of tetrahedral and octahedral sites present in the material [37]. The tetrahedral sites correspond to the bonding of positive metal ions and can be utilized during the electrochemical activity. The two peaks that occurred at 1635 and 1384 cm^{-1} are attributed to the carbonyl group (O=C) vibrations i.e., bending and stretching [38]. A strong, small band at 1036 cm^{-1} identified the C—O bond stretching vibration. These peaks were probably caused by the adsorbed ambient CO_2 or by remnants of intermediate oxalates left over after the synthesis [39]. Chemisorbed water was responsible for a large peak seen at around 3412 cm^{-1} (-OH bond). As the change in reaction time, a slight shift in the bandwidth at 557 and 648 cm^{-1} predicted a suitable Ni—O and Co—O network positioning. Variations in the peak position revealed the
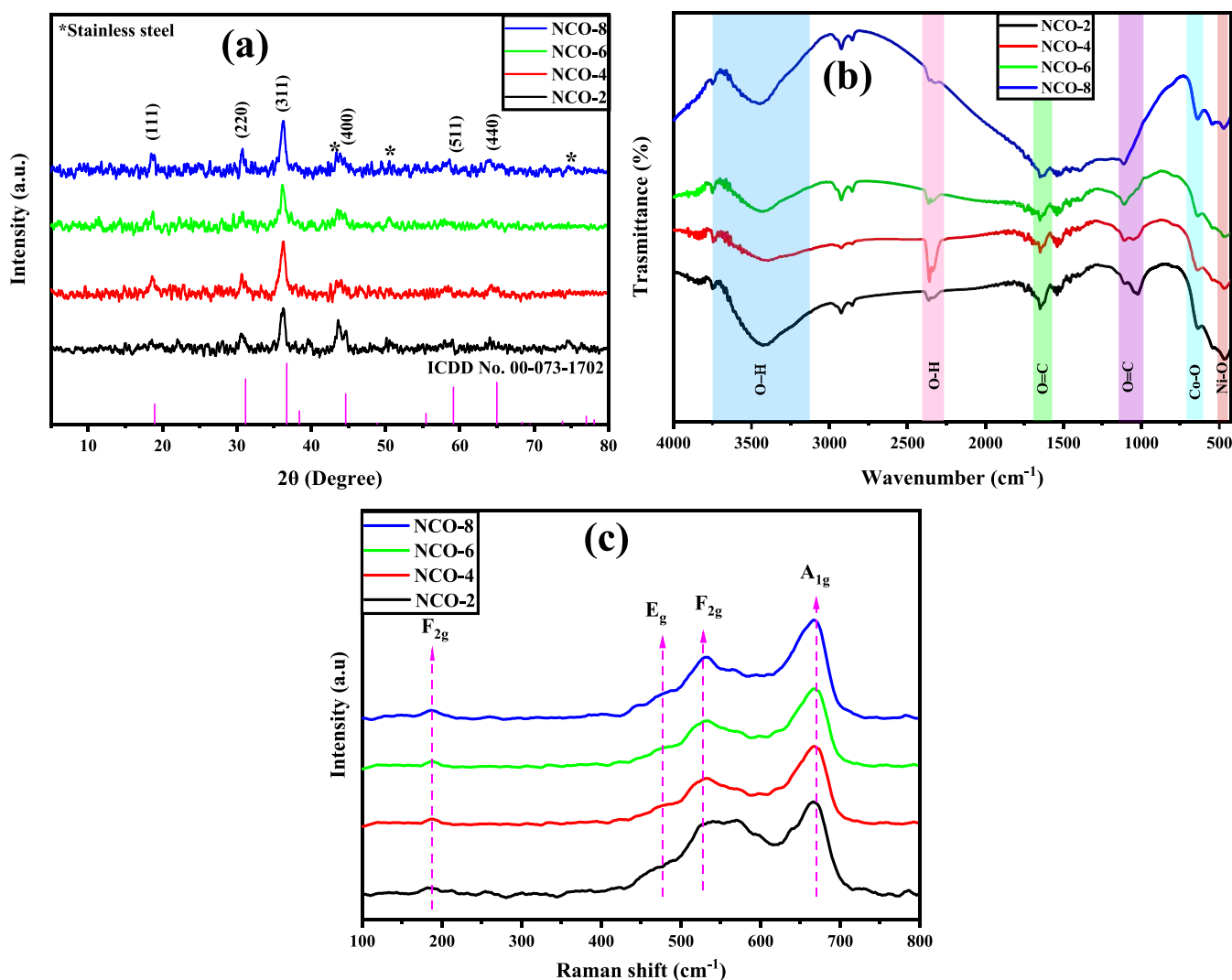

Fig. 2. (a) XRD patterns of NiCo$_2$O$_4$ films with different reaction times: NCO-2, NCO-4, NCO-6, and NCO-8 (b) FTIR spectra of NCO-2, NCO-4, NCO-6, and NCO-8 samples (c) Raman spectra of NiCo$_2$O$_4$ films with different reaction times NCO-2, NCO-4, NCO-6, and NCO-8.

increase in Ni—O and Co—O bond length, brought by the deformation of the M-O bond [40].

Raman spectra were used to further investigate the purity of the synthesized material and composition of NCO film samples, as shown in Fig. 2(c). Peaks that occurred at 186.77, 475.24, 526.47, and 669.54 cm^{-1} are associated with F_{2g}, E_g, F_{2g}, and A_{1g} phonon modes of spinel NCO phase, respectively. The peaks at 528 and 667 cm^{-1} belong to the F_g and A_{1g} phonon modes due to the vibration of the Co—O and Ni—O bond stretching, respectively [41]. The lower band (F_{2g}) corresponds to the tetrahedral sites of the material while the upper band (A_{1g}) corresponds to the octahedral sites [42]. The formation of NCO has been confirmed by these characterizations, which are more relatable to the literature [43]. The different NCO nanostructures prepared at different reaction times exhibited similar active Raman vibrational modes which confirmed the same NCO phase formation. The absence of a hydroxyl peak in the Raman spectra indicated the absence of Ni/Co hydroxide, thereby confirming the formation of NCO pure phase. This analysis is in good agreement with the XRD.

The elemental compositional analysis of NCO films was carried out by EDS. Fig. 3(a–d) shows the EDS spectra of NCO films. All NCO films i. e., NCO-2, NCO-4, NCO-6, and NCO-8 showed the presence of Ni, Co, and O in good elemental composition and revealed the deposition of NCO films. The inset chart in the EDS spectra illustrated the compositional and elemental analysis of the Ni and Co ratio with 1:2 ratio and was well matched with the stoichiometry of NCO [44]. These findings validated the formation of the spinel pure phase of NCO film and supported the results obtained from XRD and FT-IR analyses [45]

After the structural and compositional analysis, XPS was used to study the chemical composition, oxidation states, and binding energy of NCO-6 film [46]. The survey spectrum of the NCO-6 film is shown in Fig. 4(a), which confirmed the presence of Ni, Co, C, and O constituents.

The C 1s served as a reference for all XPS data analysis. The C 1s showed the highest peak at 285.6 eV. No other noticeable peak was observed in the survey spectrum which is in concurrence with EDS. The obtained compositions of Ni, Co, O, and C were 15.6 %, 31.1 %, 30.4 %, and 22.9 %, respectively. In XPS, the two doublets observed in the Ni-2p spectrum correspond to the doublets ($2p_{3/2}$ and $2p_{1/2}$) due to spin-orbit interaction, along with shakeup satellite as shown in Fig. 4(b). The Ni peak of the Ni^{3+} oxidation state is located at binding energies of 857.3 and 866.27 eV whereas, Ni^{2+} oxidation is at 884.02 eV. Also, the peaks at 860.82 and 878.80 eV, the two shakeup satellite peaks were shown in Fig. 4(b). Similarly, the Co showed two peaks at 785.61 and 801.63 eV binding energies that concern Co $2p_{3/2}$ and $2p_{1/2}$, respectively. Further, satellite peaks at 790.37 and 808.12 eV binding energies can be seen in Co core spectra [7]. Additionally, Fig. 4(c) depicts the Co 2p core-level spectrum with an energy separation of 16.24 eV indicated the existence of Co^{3+} valence state of cobalt. In fitting (Fig. 4(d)) of the O1s spectrum, the three Gaussian peaks viz. O1, O2, and O3 were observed at 532.58 eV (metal-oxygen bond), 534.97 eV (oxygen in hydroxide species), and 536.19 eV (oxygen ions in defect sites). Defects in the material with strong coupling effects lead to the positive shifting of Ni, Co, and O peaks. As a consequence of the prior discussion, it is possible to conclude that the multi-oxidation states of Ni and Co, as well as surface oxygen, contribute to improved electrochemical performance [47].

3.3. Surface and morphological study of NCO films

The surface and morphological analysis was carried out by SEM study at four different magnifications, as shown in Fig. 5. The reaction time dependence on the morphology of NCO films for NCO-2, NCO-4, NCO-6, and NCO-8 was studied from these SEM images. The diverse morphologies play a significant role in electrolyte adsorption, redox
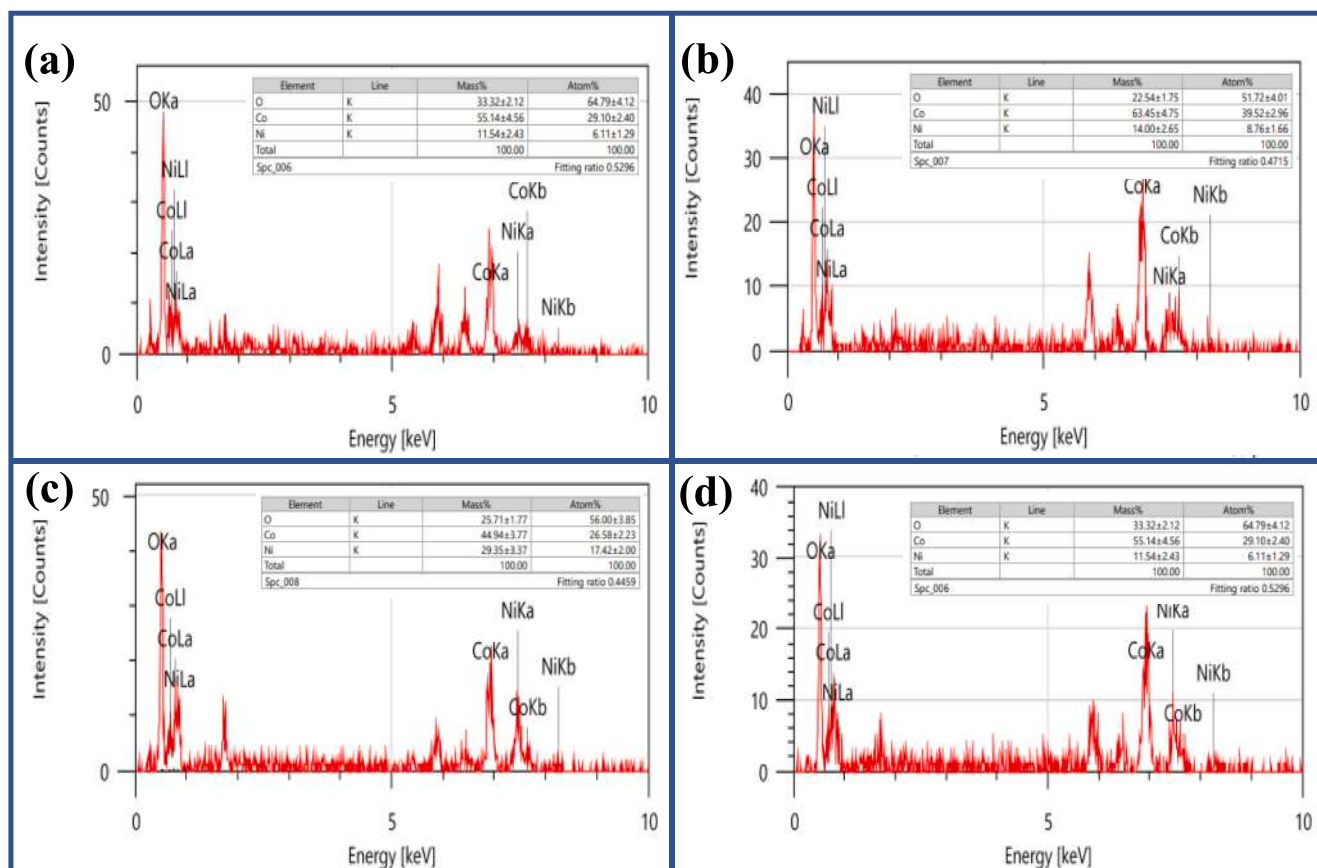

Fig. 3. EDAX images of NiCo$_2$O$_4$ films with different reaction times (a) NCO-2, (b) NCO-4, (c) NCO-6, and (d) NCO-8.
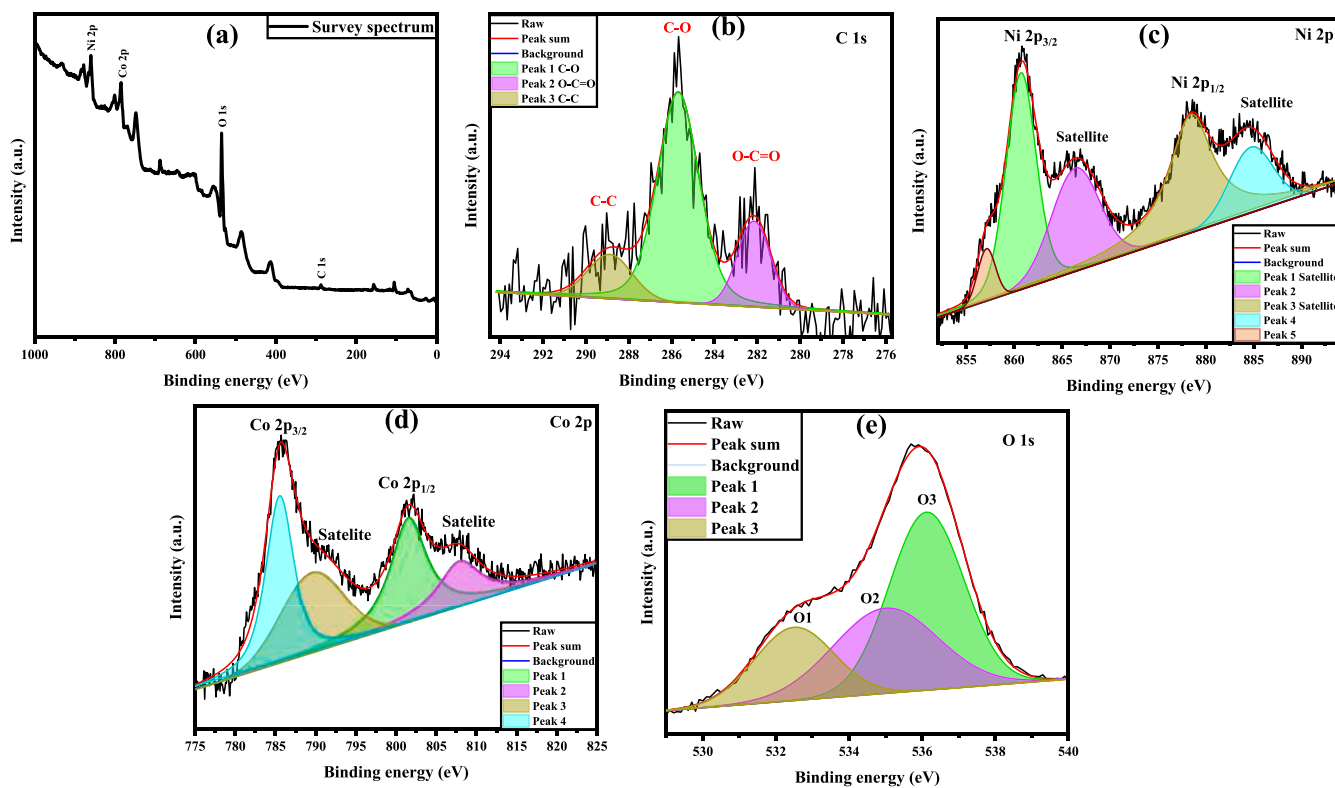
Fig. 4. XPS spectra for NiCo$_2$O$_4$ films (a) Survey spectrum, high resolution spectra of (b) C 1s, (c) Ni 2p, (d) Co 2p, and (e) O 1s.
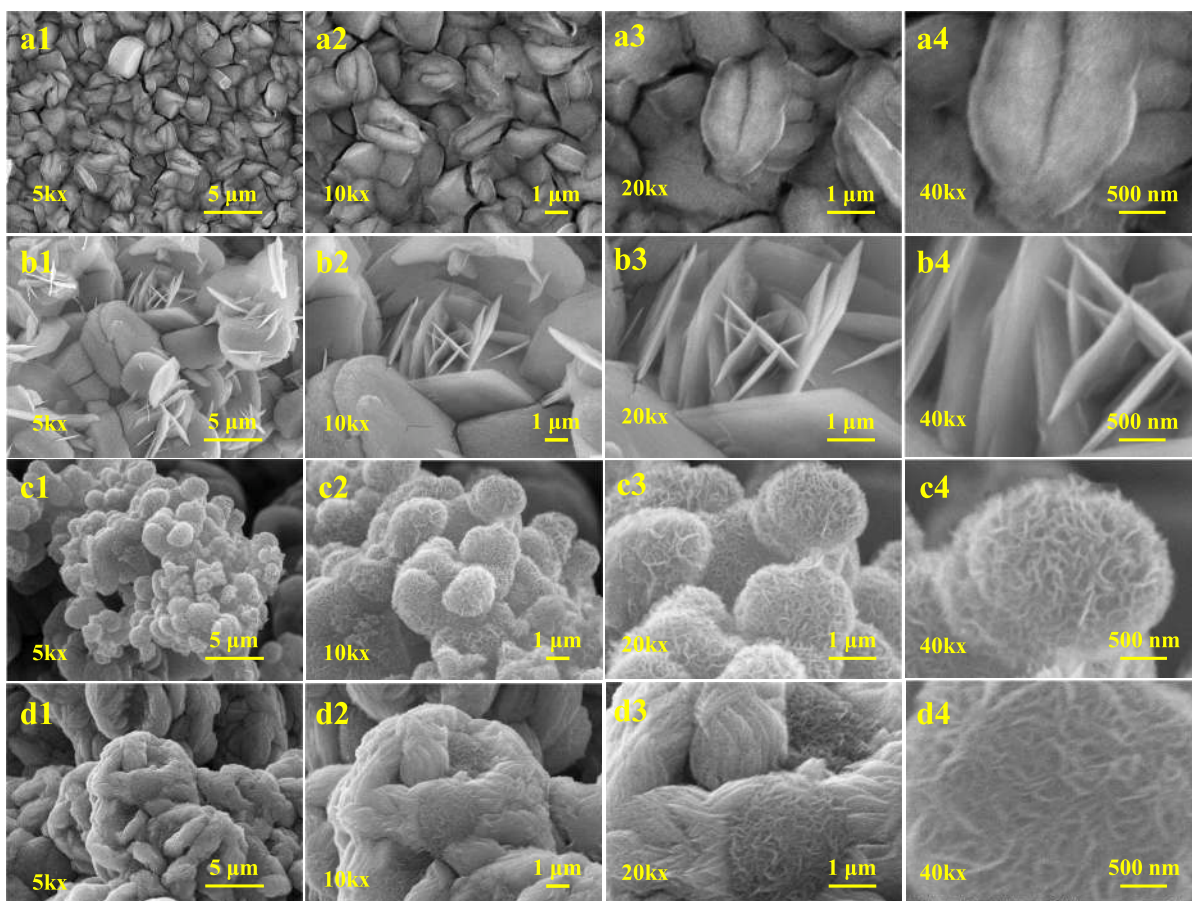

Fig. 5. SEM images of NiCo$_2$O$_4$ films with different reaction times as (a1–a4) NCO-2, (b1–b4) NCO-4, (c1–c4) NCO-6, and (d1–d4) NCO-8.

reactions, intercalation, and deintercalation into electrode material [48]. The development of superior nanostructured materials with various morphology to improve redox activities and cyclic stability of films. Fig. 5(a1–a4) shows the SEM image of NCO-2 film at different resolution which revealed wheat grain-like dense and compact nanostructure. As reaction time increased, the wheat-like structure disappeared, and formed interconnected nanoplates/nanoflakes-like morphology in the NCO-4 film as shown in Fig. 5(b1–b4). Moreover, the enhancement in reaction time transform the interconnected nanoplates to the porous self-assembled marigold flower with a size of 10–30 nm as shown in Fig. 5(c1–c4) for NCO-6 film. The marigold flower-like structure has a porous surface morphology, large active sites, and it provides an enhanced reaction rate, which is a favorable feature for SC application. Conversely, at an 8 h reaction time, the NCO-8 film exhibited compact, densely packed surfaces, reducing the electrochemical active sites, and increasing electrode diffusion resistance, as shown in Fig. 5 (d1–d4).

To get more fine insights into the structure of the NCO-6 film, the particle size and surface topography were studied using TEM. Fig. 6(a) & (b) illustrate the NCO non-uniform nanoparticles ranging in size from 25 to 45 nm, which is relatable with the SEM findings. The high-resolution TEM images (Fig. 6(c)) were used to calculate the lattice spacing of crystal planes found to be 0.32 nm for the (311) plane. The polycrystalline nature of the NCO-6 film sample can be easily seen from the Selected area electron diffraction (SAED) pattern. The large concentric circles indicate the polycrystallinity of the sample and shown in Fig. 6 (d), and validated the XRD results.

The supercapacitor tendency highly depends on the surface area of the electrode material, which can be measured from the technique as gas adsorption and desorption techniques [49]. The Brunauer-Emmett-Teller (BET) and Barrett-Joyner-Halenda (BJH) techniques were used to study the surface area and pore size of the material, as shown in Fig. 7. The powders scratched from NCO films were used for the BET study [50]. The type IV isotherm and H3 hysteresis seen in the nitrogen adsorption/desorption curves in Fig. 7(a–d) demonstrate the mesoporous nature of NCO flowers. With a comparable pore size distribution of 3–15 nm, these type IV isotherms have minor hysteresis loops,

underscoring the mesoporous structure of the NCO samples. NCO-2, NCO-4, NCO-6, and NCO-8 were found to have specific surface areas of 23.7 m^2/g, 25.1 m^2/g, 32.6 m^2/g, and 26.4 m^2/g, respectively. The formation of the microflowers was the reason behind the higher surface area of the NCO-6. Additionally, the mesoporous characteristics of $NiCo_2O_4$ powder were verified using the Barrett–Joyner–Halenda (BJH) pore size analysis, as illustrated in Fig. 7(a–d) inset. For NCO-2, NCO-4, NCO-6, and NCO-8, the average pore radii were 7.9 nm, 9.3 nm, 7.5 nm, and 8.9 nm, respectively, while the average pore volumes were 0.091 cc/g, 0.035 cc/g, 0.120 cc/g, and 0.105 cc/g, respectively. It was observed that NCO-6 had a greater surface area than NCO-2, NCO-4, and NCO-8, indicating that NCO-6 may offer more electroactive sites for the transfer of electrolyte ions. Consequently, improving the electrochemical performance of the $NiCo_2O_4$ electrode was made possible due to the mesoporous nature of the NCO-6 nanostructure. Additionally, the electrochemical performance of the NCO film can be enhanced by the mesoporous nature and marigold flower-like morphology of the NCO nanostructure, characterized by a large pore volume, short pore radius, and high specific surface area [51].

4. Electrochemical study of $NiCo_2O_4$ films

The electrochemical study of the NCO film was carried out by using a 1 M KOH electrolyte. The highly porous morphology of NCO films improved the electrochemical performance of the material due to improved mobility and redox ions activities. Fig. 8(a–d) shows the cyclic voltammetry curves of all the NCO films by different scan rates ranging from 5 to 100 mV/s with applied potential window of −0.3 to 0.5 V (vs. SCE). The CV curves exhibited quasi-rectangular shape at a lower scan rate and show small redox pairs, which confirmed the intrinsic pseudocapacitive behavior of NCO films. The presence of small redox peaks rather than clear peaks can be resulted due to the nano crystallinity and mesoporous structure of the NCO films. Due to these parameters, the surface electrochemical activities were more than the diffusion and it is also reflected in the charge contribution calculation. In an aqueous electrolyte solution, the NCO film formed oxyhydroxides of Co and Ni after going through Faradic redox reactions. The following equations
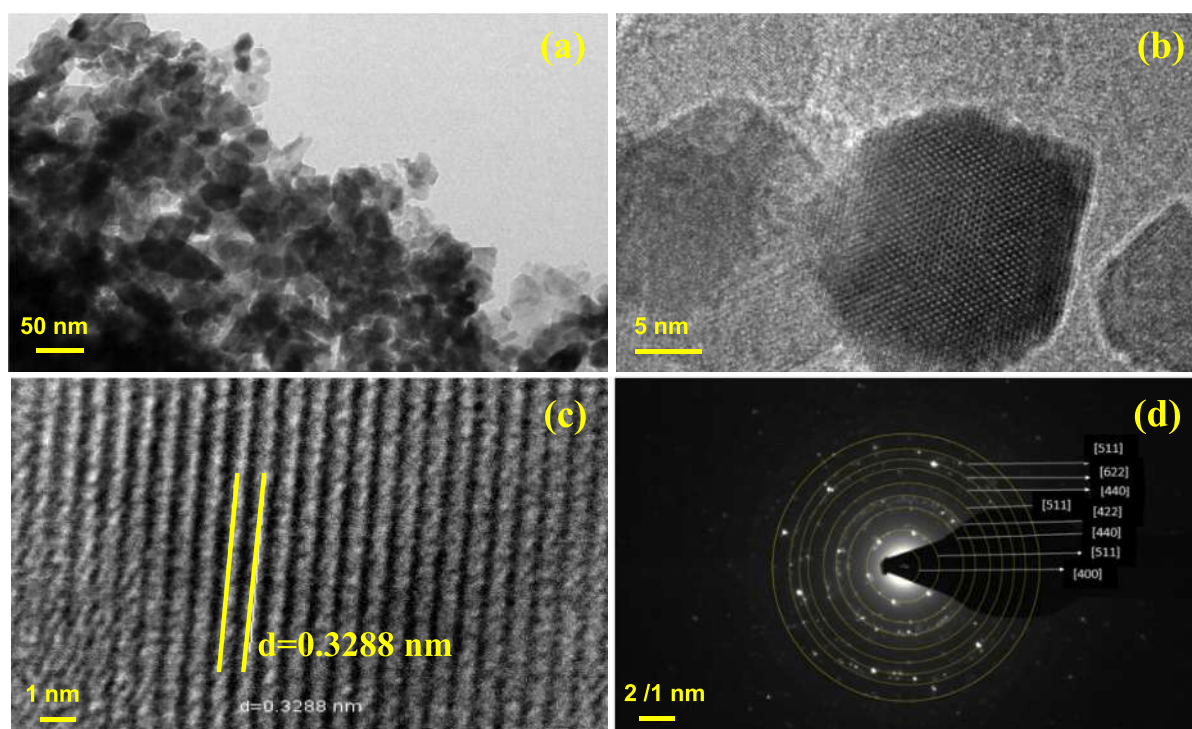

Fig. 6. a) TEM image of NCO-6 film, b) and c) HRTEM images of NCO-6 film and d) SAED pattern of NCO-6 film.
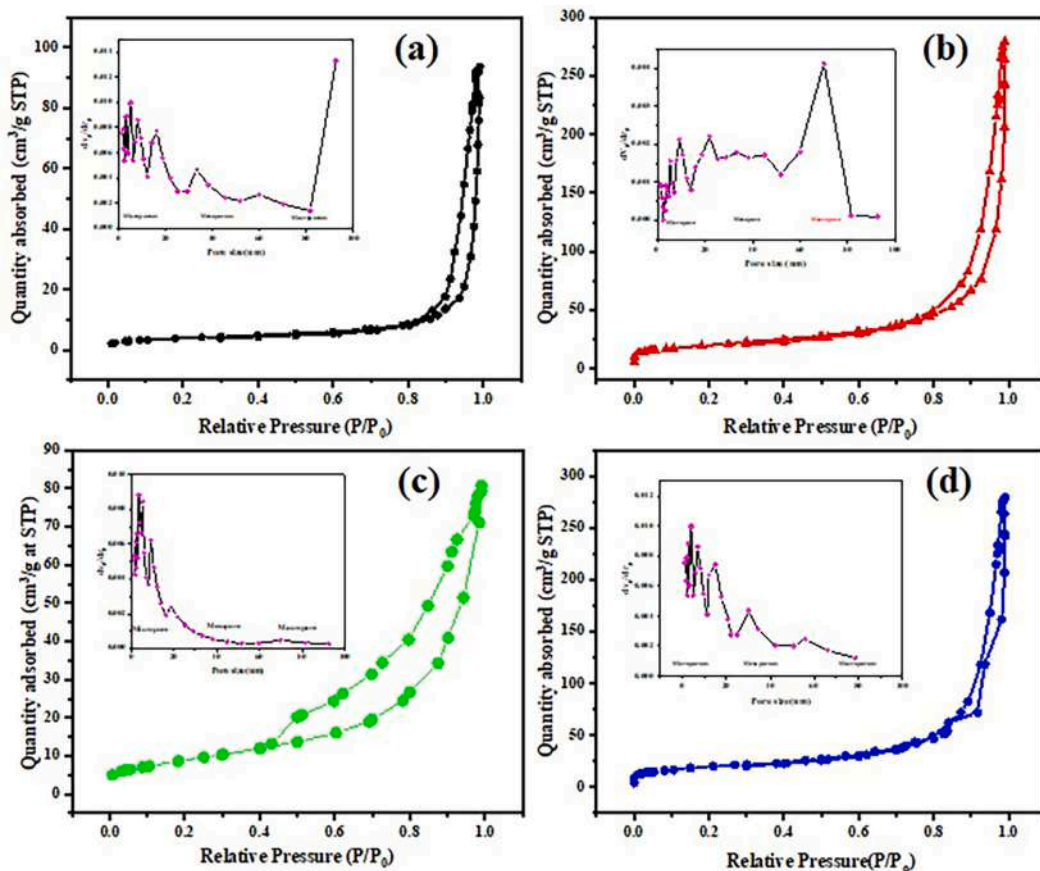
Fig. 7. Nitrogen adsorption-desorption isotherm of (a) NCO-2, (b) NCO-4, (c) NCO-6, and (d) NCO-8 (respective insets show pore size distribution of respective sample).
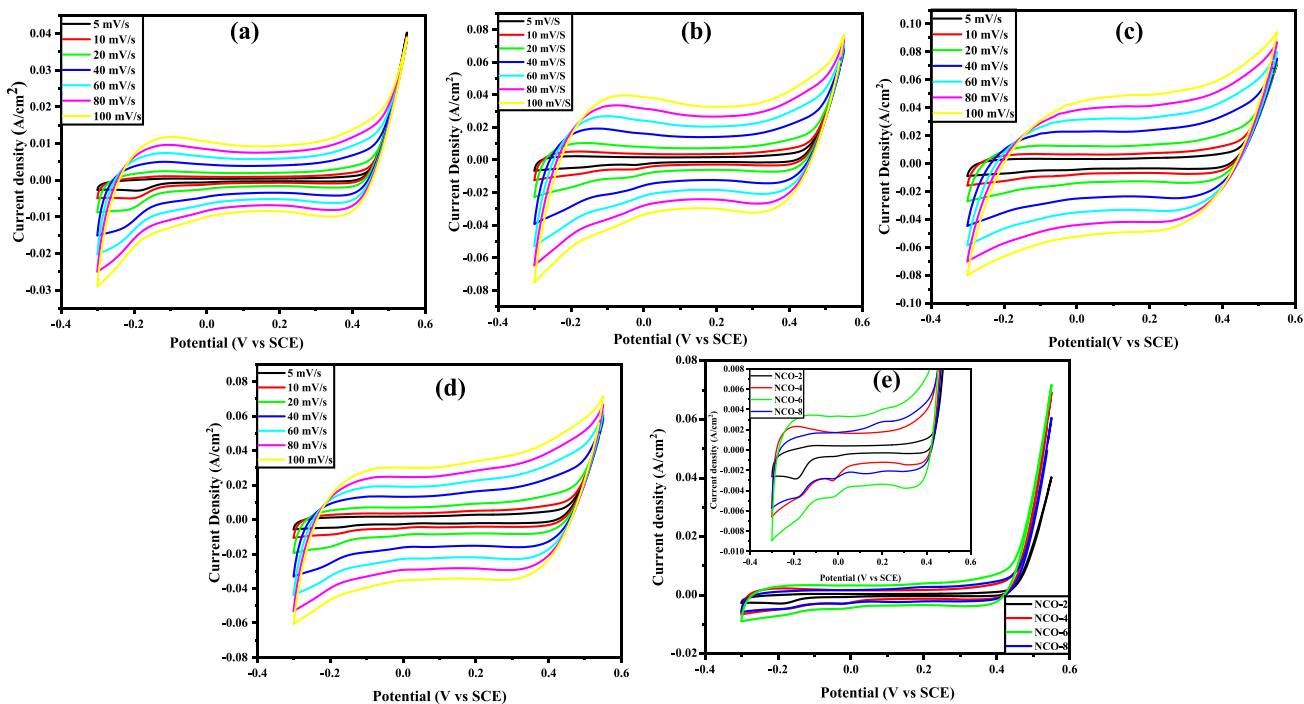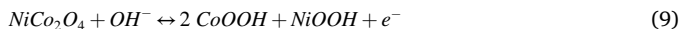

Fig. 8. CV measurement of a) NCO-2 b) NCO-4 c) NCO-6, and d) NCO-8 films. e) CV measurement of all NCO films at scan rate of 5 mV/s.

express the Faradaic reactions that occurred at during chrage storage [52],

$$NiCo_2O_4 + OH^- \leftrightarrow 2\,CoOOH + NiOOH + e^- \tag{9}$$

$$CoOOH + OH^- \leftrightarrow 2\,CoO + H_2O + e^- \tag{10}$$

$$NiOOH + OH^- \leftrightarrow NiO + H_2O + e^- \tag{11}$$

In CV curves, these peaks showed a reversible nature, which revealed the quasi-reversible process. Furthermore, as the scan rate increased, no deformation occurred in the CV indicating that the film has an excellent performance rate. The potential corresponding to the anode and cathode peaks shifted towards higher potentials as the scan rates increased due to fast faradaic electrode-electrolyte reactions. As scan rate increased, peak current also increased. The redox peaks shifted towards higher potentials, indicating rapid ion and electron transport within the film, as shown in Fig. 8. The CV curve area increased up to the NCO-6 sample; thereafter, it decreased as the crystal size increased. Fig. 8(e) shows the CV curve of all NCO samples at a 5 mA/cm^2 scan rate. This led to an understanding that, in comparison to the other sample, NCO-6 has a higher area under the curve. So, the low crystalline size in the NCO-6 sample helped in the intercalation/deintercalation of electrolyte ions [53]. The current relation with scan rate was investigated by using power law to differentiate the charge storage behaviors and is shown in Fig. 9(a),

$$i = a\,v^b \tag{12}$$

where, peak current (i), scan rate (v), intercept (a), and slope (b) are determined from the graph of log (i) vs. log (v). The b value varied from 0.5 to 1, which implied the mixed processes as surface redox reactions and diffusion in the NCO films. The electrochemical kinetics analysis can quantify the contributions of each film that included both diffusion-controlled and capacitive charge storage processes and are given by the following equations [54],

$$Q_t = Q_s + C\,v^{-1/2} \tag{13}$$

$$Q_t = Q_s + Q_d \tag{14}$$

where, total charge (Q_t), surface capacitive charge (Q_s), diffusion charge (Q_d), constant (c), and scan rate (v). The Q_s can be calculated from Q_t vs $v^{-1/2}$ plot [55]. The Fig. 9(b) shows the capacitive and diffusion-controlled contributions of NCO-2, NCO-4, NCO-6, and NCO-8 films. The NCO films showed Q_s distribution of 93.83, 74.15, 52.69, and 65.54 % at 5 mV/s, whereas, Q_d distribution was observed at lower scan rates of 6.15, 25.84, 47.30, and 34.45 % at 5 mV/s for NCO-2 to NCO-8 films. Especially, NCO-6 film demonstrated nearly equal contribution of capacitive and diffusion controlled and also higher diffusion than other NCO films. Fig. 9(c) shows that the diffusion-controlled contribution of the NCO-6 films decreased as the scan rate increased. This could be have happened because the interaction time of the ions at higher scan rates is very less.

The NCO charge-discharge characteristics were studied by the GCD technique. GCD measurements of synthesized NCO films in a 1 M KOH
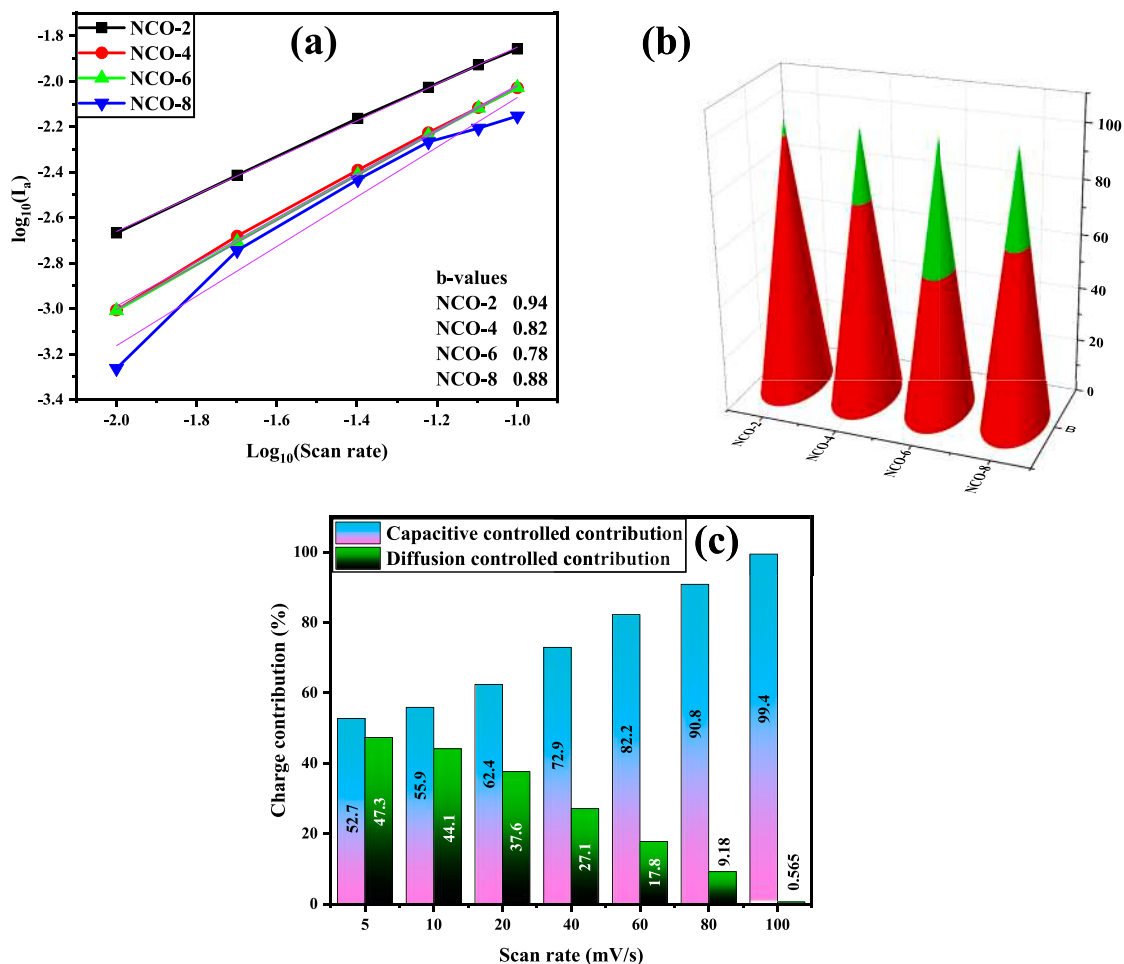

Fig. 9. a) Graph of $\log_{10}(I_a)$ vs $\log_{10}$(scan rate) (inset table of b value), b) 3D Plot of diffusion controlled and capacitive controlled contribution of all samples and (c) Charge contribution plot of NCO-6 film.

electrolyte to further appraise the C_s. The measurements were taken by applying a potential range of −0.3 to 0.4 V at 5 to 25 mA/cm² as shown in Fig. 10(a–d). The potential window used in CV analysis is not applicable directly to the analysis of GCD profiles because electrode material supersaturation occurred within the prescribed CV potential window. As a result, the voltage range for GCD analysis is modified appropriately. The higher potential from 0.5 V to 0.4 V was reduced to offer the best feasible window for GCD analysis [56]. Fig. 10(e) suggests that NCO-6 has greater discharge time as compared with other samples. The less active material participation in redox reactions leads to the voltage drop at higher current densities which causes a decrease in C_{sp} [57]. The calculated C_{sp} from Eq. (1) were 233, 536, 1277, and 862 F/g at 5 mA/cm² for NCO-2, NCO-4, NCO-6, and NCO-8, respectively. Fig. 11(a) shows the capacitance variation of the NCO films at various current densities, in which the specific capacitance decreased as current density increased for all samples. Fig. 11(b) and (c) show the Ragone plot and Coulombic efficiency of NCO films, respectively. The NCO-6 film showed the highest Coulombic efficiency as compared with others. The rate capabilities of the electrode can give the information about storage ability of the material at higher current densities. Rate capabilities of the NCO-6 were 63, 58, 52, and 49 % at 10, 15, 20, and 25 mA/cm², respectively. The NCO-6 showed a higher rate capability of 63 % at 10 mA/cm² with 811 F/g specific capacitance. The rate capability was decreased as the current density increased. Table 1 shows a comparison of electrochemical performance of NCO films while, comparison of NCO films with the existing literature is shown in Table 2.

EIS was used to study the electrical and dielectric properties of the NCO films. The Nyquist plot was carried out at 0.1 Hz to 10^5 Hz frequency range, shown in Fig. 12(a). All the NCO films showed semicircles and a straight line at high and low-frequency regions, respectively. The series resistance (R_s) calculated from the EIS plot were 1.31, 0.61, 0.76, and 2.03 Ω. Whereas, the charge transfer resistance (R_{ct}) values were 0.68, 0.81, 0.71, and 1.17 Ω for all NCO films. The NCO-6 film with the lowest R_{ct} value suggested that ionic and electronic conductivity was effectively enhanced due to binder free synthesis [58]. Based on the EIS measurements, the NCO-6 film showed outstanding electrochemical behavior.

The GCD technique was used to perform the cyclic stability of synthesized NCO-6 film. The 75 mA/cm² current density was used to study the cyclic stability over 10,000 GCD cycles. Fig. 12(b) reveals the retention in capacitance of NCO-6 film over 10,000 cycles. After 10,000 GCD cycles, the stability plot for the NCO-6 film revealed 95 % capacitance retention, only a 5 % decline in capacitance which might have occurred due to material degradation in an aqueous electrolyte. The intercalation and deintercalation of electrolyte ions during charge-discharge cycles to counterbalance the overall charge could also introduced mechanical stress to the physical structure of the film material [59]. In addition to redox reactions that would result in composition destruction due to irreversible chemical reactions. A recurrent charge-discharge operation would undoubtedly result in mechanical and electrical problems that reduce the initial performance due to the loss of active material mass [60]. To investigate the effect of cycling, XRD pattern of NCO-6 film was studied after cycling stability and is shown in Fig. 12(c). From the XRD patterns of before and after stability, it was seen that there are no large changes in the material's structural properties and phase. Fig. 12(d) graph reveals a radar plot which suggests that NCO-6 film has outstanding performance. The Table 2 shows the comaprasion of the NCO performance with other reported materials.

5. Aqueous symmetric supercapacitor (ASS) device

The ASS device was fabricated using NCO-6 film as both the anode and cathode were immersed in a 1 M KOH solution. Each electrode had a mass loading of 2.9 mg in the symmetric supercapacitor configuration. In the two-electrode experiments, the NCO//NCO device exhibited positive electrochemical active potential window ranging from 0.0 to 1.6 V vs SCE. To determine the optimum potential window, the potential range was varied from 1.0 V to 1.6 V at a scan rate of 100 mV/s, as illustrated in Fig. 13(a). The ASS device operated in a maximum voltage window of 1.6 V. Fig. 13(b) depicts CV curves of an NCO//NCO ASS device at various scan rates in the 1.6 V potential range. At higher scan rates, the CV curves replicated their shapes which indicated the rapid
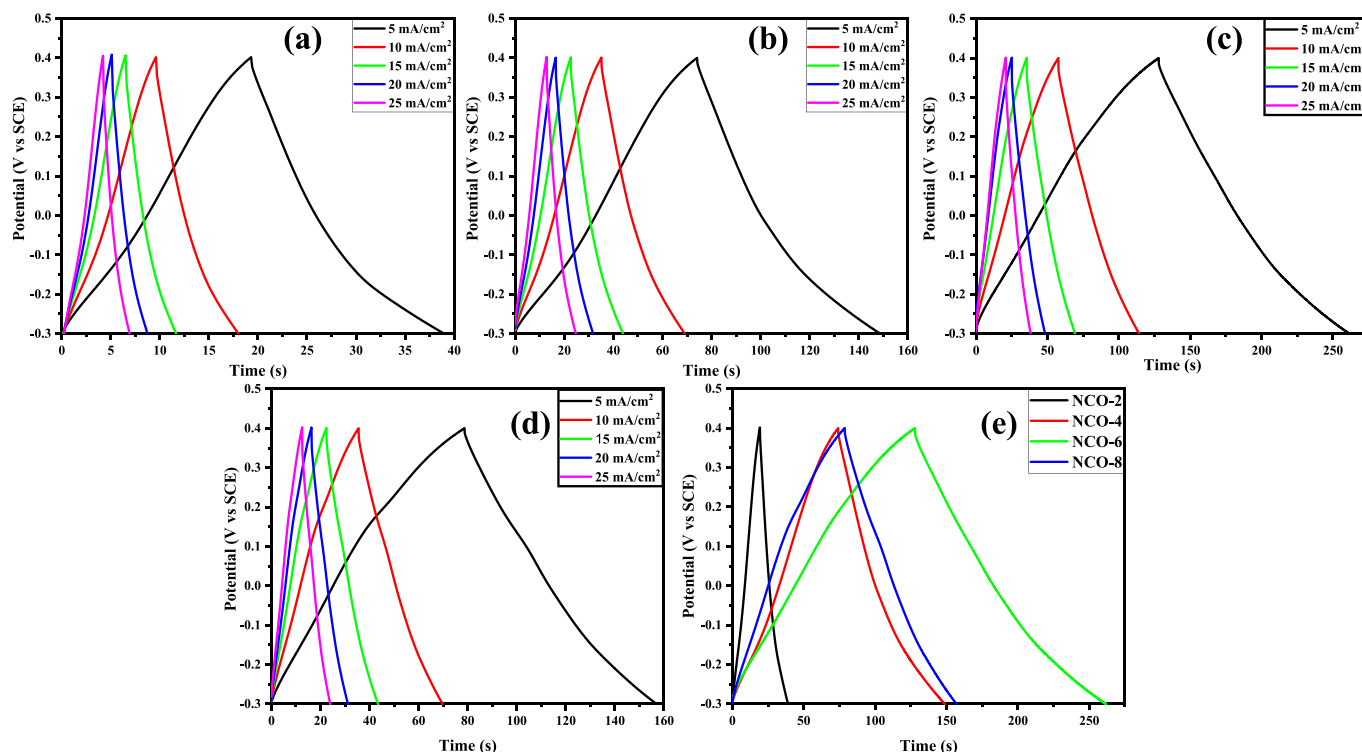

Fig. 10. GCD measurement of a) NCO-2 b) NCO-4 c) NCO-6 and d) NCO-8 films. e) GCD curves of all NCO films at current density of 5 mA/cm².
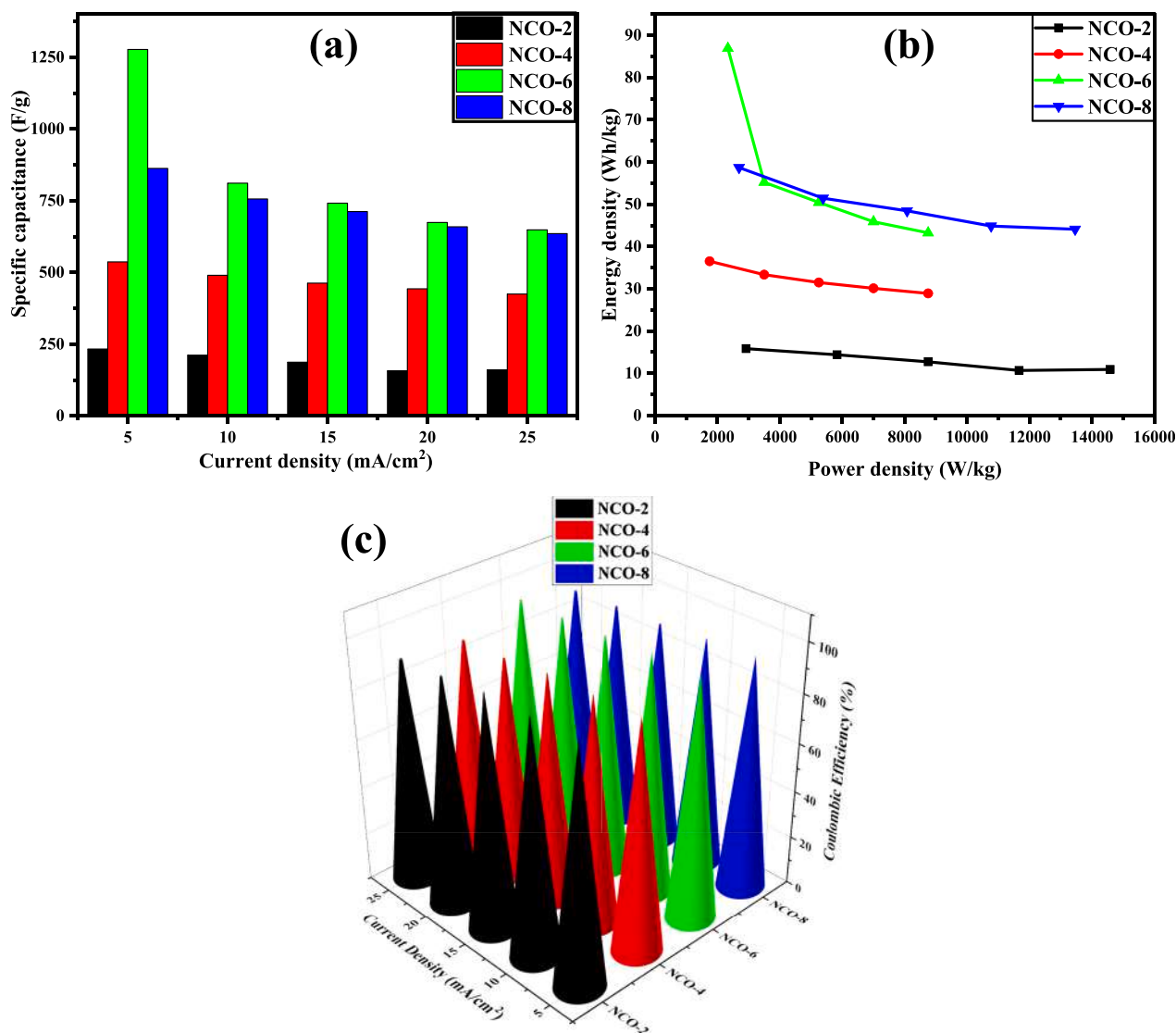
Fig. 11. a) Specific capacitance vs current density, (b) Ragone plot and (c) 3D Plot of Coulombic efficiency vs current density of NCO films.

Table 1

Comparative table showing the structural and supercapacitive properties of NCO films at 5 mA/cm^2 current density.

Sr. No.	Sample code	Mass loading (g)	Discharge time (s)	Specific capacitance (F/g)	Energy density (Wh/kg)	Power density (W/kg)	Rate capability (%)
1	NCO-2	0.6	19.5	233	15	2916	91
2	NCO-4	0.65	78.5	862	58	2692	87
3	NCO-6	0.75	134.1	1277	86	2333	63
4	NCO-8	1.01	75.1	536	36	1750	89

kinetics in a redox reaction. This phenomenon indicated the device's capability for efficient charge storage and release, crucial for applications requiring high power output or rapid energy transfer.

The GCD tests were conducted to explore the charge storage capabilities and rapid delivery of the ASS device, as delineated in Fig. 13(c). The NCO//NCO ASS device demonstrated quasi-linear behavior with extended charge-discharge periods across all current densities, indicating its pseudocapacitive properties and exceptional energy storage capacity. Notably, at a current density of 2 mA/cm^2, the NCO//NCO ASS device exhibited a specific capacitance (C_s) of 45.68 F/g, underscoring its ability to efficiently store charge. Furthermore, the ASS device yielded an energy density of 16.24 Wh/kg and a power density of 275.86 W/kg at 2 mA/cm^2, reflecting its robust performance across various operational parameters. These metrics highlighted the device's capability to store substantial energy while delivering power rapidly, a crucial aspect for applications demanding high-performance energy storage solutions.

Furthermore, the NCO//NCO ASS device exhibited outstanding and durable electrochemical performance, retaining up to 90.5 % of its capacity after 5000 cycles at a current density of 15 mA/cm^2, as depicted in Fig. 13(d). This remarkable retention underscores the device's suitability for high-energy and power applications, where long-term stability and consistent performance are paramount. To assess the device's stability and internal resistance, EIS was conducted before and after the cycling stability test [48]. As shown in Fig. 13(e), the R_s values for the NCO//NCO ASS device before and after stability were 0.603 and 0.615

Table 2

Comparison of performance metrics of synthesized NCO film with other reported literature.

| Sr. No.	Material	Methods	Morphology	Specific capacity/capacitance	Stability	Energy density (Wh/kg)	Power density (W/kg)	Ref.
1	$NiCo_2O_4$	CBD	Nanoflowers with nanorods	702 F/g	94.2 % after 5000 cycles	18.52	313	[23]
2	$NiCo_2O_4$	Electrodeposition	Nanosheets	1730 F/g	80 % after 5000 cycles	56	349	[61]
3	$NiCo_2O_4$	Hydrothermal	Nanowire	1183 mF/cm^2	90.4 % after 3000 cycles	24	–	[62]
4	$NiCo_2O_4$	CBD	Marigold micro-flower like	530 F/g	90.5 % after 3000 cycles	41.66	3000	[24]
5	$NiCo_2O_4$	Electrospinning and hydrothermal	Nanoneedle	910 F/g	88 % after 1000 cycles	40.81	738	[63]
6	$NiCo_2O_4$/ MnO_2	Two-step electrodeposition method	Core–shell nanosheets	3.81 F/cm^2	86.1 % after 10,000 cycles	25	–	[64]
7	$NiCo_2O_4$	Hydrothermal	Nanoflakes, nanoflowers	1030 F/g	–	10	2000	[65]
8	$CuCo_2O_4$	Solvothermal	Marigold flower	627C/g	95 % after 5000	–	–	[66]
9	$CuCo_2O_4$	Hydrothermal	Non uniform spherical microstructure	193 F/g	85.9 % after 6000	2.12	227	[67]
10	$CuCo_2O_4$	Hydrothermal	Nanowire, nanosheet	299.12C/g	100 % after 5000	36.46	1003	[68]
11	$MgCo_2O_4$	Solvothermal	Microsphere	375.5C/g	100 % after 6000	35.4	8905	[69]
12	$MnCo_2O_{4.5}$	Hydrothermal	Nanosheet	304.37C/g	100.04 % after 5000	30.36	950.83	[70]
13	$MnCo_2O_{4.5}$	Solvothermal	Microflower	287.02C/g	100 % after 5000	30.33	959.35	[71]
14	β-$Co(OH)_2$	Solvothermal	Microflower, microclews	396.5C/g	100 % after 5000	43.6	989.3	[72]
15	$NiCo_2O_4$	CBD	Wheat grain into marigold micro flowers	1277 F/g	95 % after 10,000	86	2333	This Work
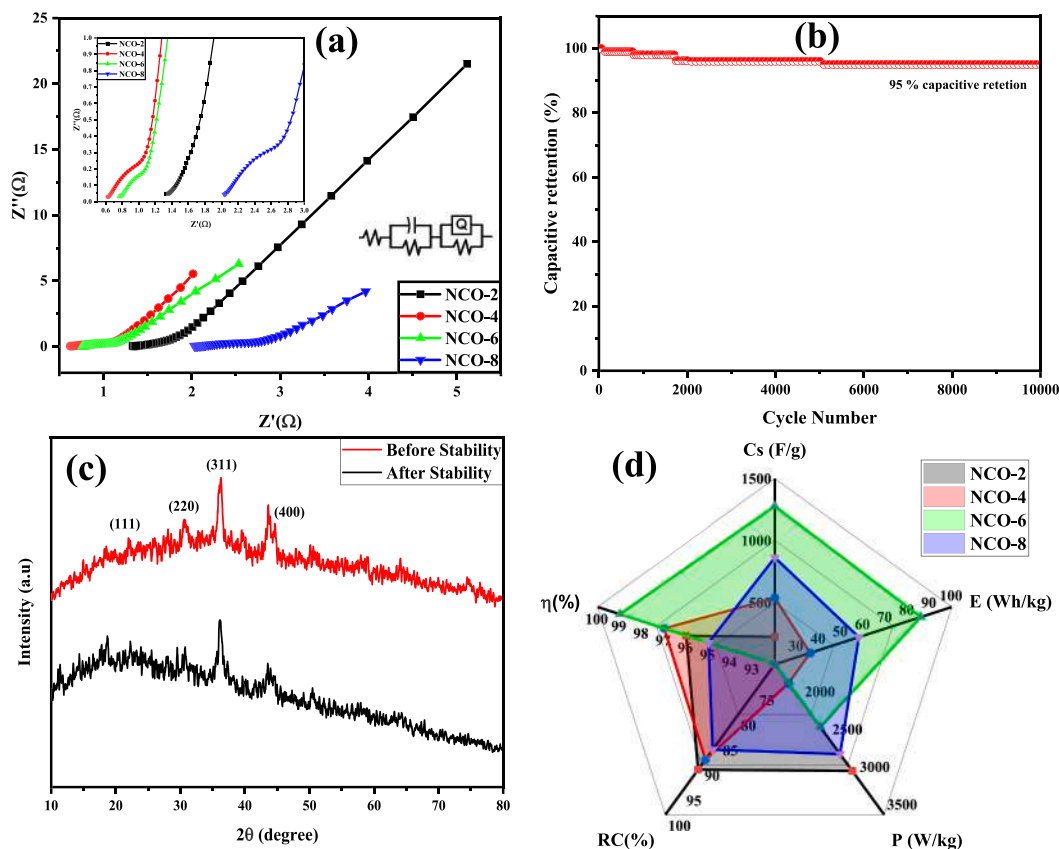
Fig. 12. (a) Nyquist plot with circuit fitting by ZsimpWin software (b) Cycling stability graph of NCO-6 (c) XRD plot before and after cyclic stability, and (d) Radar plot of various supercapacitor metrics of all the NCO films.

Ω, respectively. Moreover, R_{ct} changed from 1.28 to 1.39 Ω. The low R_s and R_{ct} values were observed in the NCO//NCO ASS device and, indicated the pivotal role of intercalation processes in enhancing charge transfer kinetics through improved conductivity and rapid ion diffusion within the electrochemical system. Table 3 gives the comparative glance of the NCO//NCO device with other reported symmetric devices. This underscored the device's efficiency in facilitating seamless charge transfer and ion transport, contributing to its robust electrochemical performance and long-term stability.
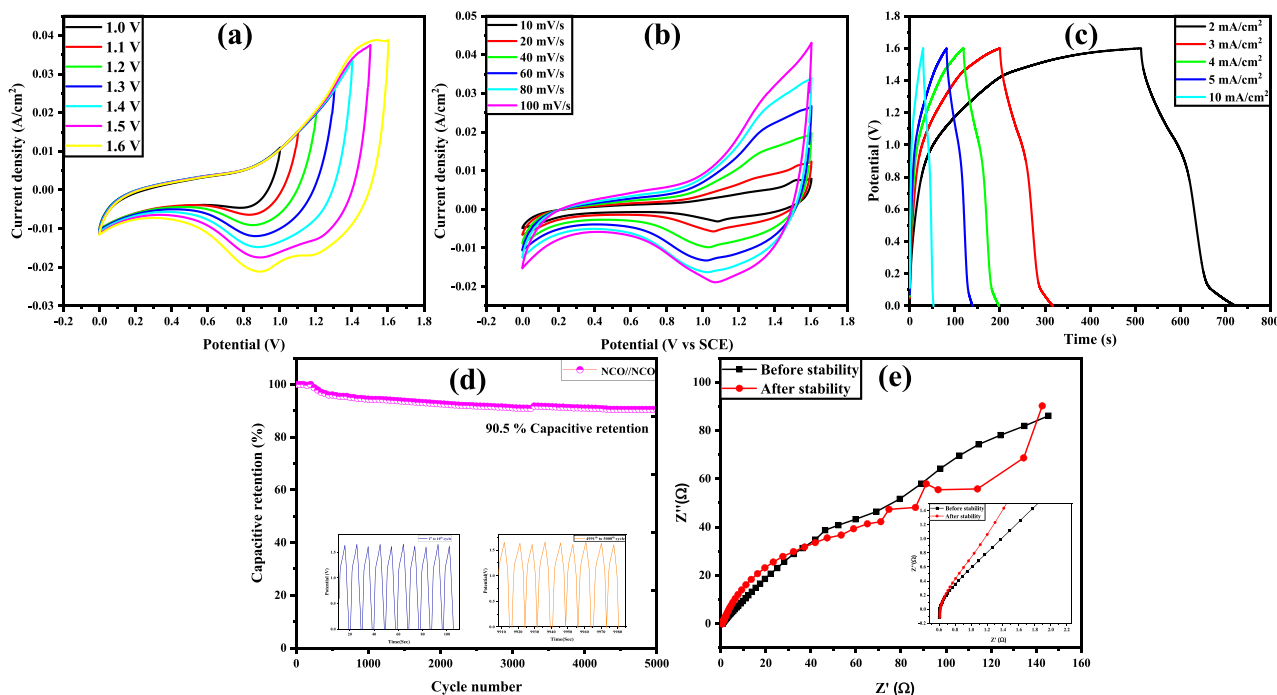
Fig. 13. (a) CV at different potential window (b) CV of NCO//NCO ASS device at different scan rate (c) GCD of NCO//NCO ASS device at different current densities (d) stability graph of NCO//NCO ASS (inset plot shows charge discharge vs time for 1st 10 cycle and last 10 cycles) and (e) Nyquist plot before and after stability.

Table 3
Comparison of performance metrics of aqueous symmetric supercapacitor devices with other reported literature.

Sr. No.	Material for symmetrical devices	Electrolyte	Sp. capacitance (F/g)	Energy density (Wh. kg)	Power density (W/kg)	Stability	Ref.
1	PANI/VG/Ti//PANI/VG/Ti	0.5 M H_2SO_4	320	26.1	383	86 % after 10,000 cycles	[73]
2	N-rGO//N-rGO	0.5 M K_2SO_4	–	128	113	96.5 % after 10,000 cycles	[74]
3	N-AC/Gr//N-AC/Gr	6 M KOH	–	13.1	12.5	93 % after 10,000 cycles	[75]
4	RCFs//RCFs	1.0 M N_2SO_4	52	6.1	160	93.6 % after 10,000 cycles	[76]
5	CSCs//CSCs	0.5 M H_2SO_4	307	8.8	4083	100 % after 10,000 cycles	[77]
6	NCO//NCO	1 M KOH	45.86	16.24	275.8	90.5 % after 5000 cycles	This work

6. Conclusion

Nickel cobaltite films were successfully fabricated using the CBD approach on a stainless-steel substrate. The XRD analyses confirmed the synthesis of $NiCo_2O_4$ film. FT-IR and FT-Raman spectroscopy confirmed the presence of metal oxides as Ni—O and Co—O bonds in the NCO films. SEM revealed the porous 3D-nanostructured marigold flower-like morphology of NCO-6 film which offered more electroactive sites for electrochemical reactions as compared to the other NCO films. The NCO-6 sample showed the 32.6 m^2/g specific surface area. The electro-chemical analysis revealed that at 5 mA/cm^2, the NCO-6 film had an excellent specific capacitance of 1277 F/g. The NCO-6 film is a promising option due to its outstanding C_{sp}, high energy density, high power density, and cyclic stability of 95 % over 10,000 cycles. Additionally, an ASS (NCO//NCO) showed higher C_{sp} of 45.68 F/g at 2 mA/cm^2 with energy density and power density of 16.24 Wh/kg and 275.86 W/kg at 2 mA/cm^2, respectively. The device exhibited superior capacitance retention of 90.5 % over 5000 galvanostatic charge-discharge cycles. Based performance, the marigold microflower-like nanostructures produced by the aforementioned synthetic technique can provide a new pathway for the fabrication of energy storage devices for both high energy density and high power density. Hence, these results could be useful for developing high-performance supercapacitor electrode material.

CRediT authorship contribution statement

P.S. Naik: Writing – review & editing, Writing – original draft, Visualization, Validation, Methodology, Investigation, Data curation, Conceptualization. **R.S. Redekar:** Writing – review & editing, Writing – original draft, Visualization, Validation, Software, Methodology, Investigation, Data curation. **Jayashri V. Kamble:** Writing – review & editing, Writing – original draft, Validation, Methodology, Investigation, Data curation, Conceptualization. **K.V. Patil:** Writing – review & editing, Formal analysis. **S.N. Tayade:** Formal analysis. **V.L. Patil:** Formal analysis. **N.L. Tarwal:** Supervision, Resources, Project administration. **M.M. Karanjakar:** Supervision, Resources, Project administration, Funding acquisition. **P.D. Kamble:** Supervision, Resources, Project administration, Funding acquisition.

Declaration of competing interest

The authors declare that they have no known competing financial interests or personal relationships that could have appeared to influence the work reported in this paper.

Data availability

No data was used for the research described in the article.

References

[1] P. Simon, Y. Gogotsi, Perspectives for electrochemical capacitors and related devices, Nat. Mater. 19 (11) (2020) 1151–1163.

[2] R. Redekar, A. Avatare, J. Chouhan, K. Patil, O. Pawar, S. Patil, et al., Review on recent advancements in chemically synthesized manganese cobalt oxide ($MnCo_2O_4$) and its composites for energy storage application, Chem. Eng. J. 450 (2022) 137425.

[3] O.Y. Pawar, S.L. Patil, R.S. Redekar, S.B. Patil, S. Lim, N.L. Tarwal, Strategic development of piezoelectric nanogenerator and biomedical applications, Appl. Sci. 13 (5) (2023) 2891.

[4] D.P. Dubal, P. Gomez-Romero, B.R. Sankapal, R. Holze, Nickel cobaltite as an emerging material for supercapacitors: an overview, Nano Energy 11 (2015) 377–399.

[5] S.B. Dhavale, V.L. Patil, S.A. Beknalkar, A.M. Teli, A.H. Patil, A.P. Patil, et al., Study of solvent variation on controlled synthesis of different nanostructured $NiCo_2O_4$ thin films for supercapacitive application, J. Colloid Interface Sci. 588 (2021) 589–601.

[6] K. Patil, R. Redekar, A. Bhoite, P. Patil, J. Jang, N. Tarwal, Multifunctionality of chemically synthesized quaternary copper nickel tin sulfide (Cu_2NiSnS_4) compound, Sustain. Mater. Technol. 39 (2023) e00775.

[7] A. Yadav, R. Redekar, K. Patil, V. Kshirsagar, N. Tarwal, Development of the nickel foam supported hydrothermally grown binder-free and highly porous magnesium-cobalt hydroxide films for supercapacitor application, Journal of Energy Storage. 81 (2024) 110292.

[8] S. Jin, I. Ryu, G. Choe, S.W. Song, H.M. Kim, D. Hong, et al., Trade-off between areal capacitance and optical transmittance of highly transparent MnO_2 electrodes for supercapacitors, Journal of Energy Storage. 50 (2022) 104641.

[9] A. Bhoite, K. Patil, R. Redekar, J. Jang, V. Sawant, N. Tarwal, Recent advances in Metal-Organic Framework (MOF) derived metal oxides and their composites with carbon for energy storage applications, Journal of Energy Storage 72 (2023) 108557.

[10] S. Khavale, R. Ambare, U.T. Nakate, B. Lokhande, Potentiodynamic electrodeposited $MnO2$: Co_3O_4 thin films electrodes for supercapacitor application, J. Mater. Sci. Mater. Electron. 34 (17) (2023) 1345.

[11] Q. Chen, R. Guo, Y. Jiang, L. Li, W. Qin, Y. Tan, et al., Facile preparation of $CoMoO_4/NiCo_2O_4$ nano-sphere anode materials and their performance in asymmetric supercapacitors, Chem. Eng. Sci. 284 (2024) 119436.

[12] M. Pathak, S.M. Jeong, C.S. Rout, Spinel $NiCo_2O_4$ based hybrid materials for supercapacitors: recent developments and future perspectives, Journal of Energy Storage 73 (2023) 108881.

[13] B. Sahoo, V. Pandey, A. Dogonchi, P. Mohapatra, D. Thatoi, N. Nayak, et al., A state-of-art review on 2D material-boosted metal oxide nanoparticle electrodes: supercapacitor applications, Journal of Energy Storage 65 (2023) 107335.

[14] S. Naeem, A.V. Patil, A.V. Shaikh, U. Shinde, D. Husain, M.T. Alam, et al., A review of cobalt-based metal hydroxide electrode for applications in supercapacitors, Adv. Mater. Sci. Eng. 2023 (2023).

[15] M. Mustaqeem, G.A. Naikoo, M. Yarmohammadi, M.Z. Pedram, H. Pourfarzad, R. A. Dar, et al., Rational design of metal oxide based electrode materials for high performance supercapacitors–a review, Journal of Energy Storage 55 (2022) 105419.

[16] M. Zheng, X. Xiao, L. Li, P. Gu, X. Dai, H. Tang, et al., Hierarchically nanostructured transition metal oxides for supercapacitors, Sci. China Mater. 61 (2) (2017) 185–209.

[17] S. Kumar, A. Tahira, A.L. Bhatti, M.A. Bhatti, Z.A. Ujjan, U. Aftab, et al., Oxygen vacancies and tailored redox activity encountered with $NiCo_2O_4$ nanostructures for promising applications in supercapacitor and water oxidation, Journal of Energy Storage 77 (2024) 109994.

[18] X. Wang, C. Deng, X. Hong, W. Dong, B. Liang, Controllable synthesis of $NiCo_2O_4$, $NiCo_2O_4$/graphene composite and their electrochemical application in supercapacitors, Journal of Energy Storage 55 (2022) 105837.

[19] D. Wang, Q. Mi, H. Zhang, G. Li, D. Zhang, Sensitive xylene gas sensor based on $NiO-NiCo_2O_4$ hierarchical spherical structure constructed with nanorods, IEEE Sensors J. 22 (11) (2022) 10346–10352.

[20] Q. Abbas, H. Khurshid, R. Yoosuf, J. Lawrence, B.A. Issa, M.A. Abdelkareem, et al., Engineering of Nickel, Cobalt Oxides and Nickel/Cobalt Binary Oxides by Electrodeposition and Application as Binder Free Electrodes in Supercapacitors, 2023.

[21] D. Pereverzev, I. Giniyatullin, E. Vladimirova, V. Zhuravlev, A. Dmitriev, Influence of the synthesis method on the morphology, dispersion and porosity of nanostructured powders of nickel–cobalt spinel $NiCo_2O_4$, J. Sol-Gel Sci. Technol. 103 (3) (2022) 935–942.

[22] R.R. Salunkhe, K. Jang, H. Yu, S. Yu, T. Ganesh, S.-H. Han, et al., Chemical synthesis and electrochemical analysis of nickel cobaltite nanostructures for supercapacitor applications, J. Alloys Compd. 509 (23) (2011) 6677–6682.

[23] R. Waghmode, N. Maile, D. Lee, A. Torane, Chemical bath synthesis of $NiCo_2O_4$ nanoflowers with nanorods like thin film for flexible supercapacitor application-effect of urea concentration on structural conversion, Electrochim. Acta 350 (2020) 136413.

[24] G.P. Kamble, A.A. Kashale, A.S. Rasal, S.A. Mane, R.A. Chavan, J.-Y. Chang, et al., Marigold micro-flower like $NiCo_2O_4$ grown on flexible stainless-steel mesh as an electrode for supercapacitors, RSC Adv. 11 (6) (2021) 3666–3672.

[25] A.R. Liandi, A.H. Cahyana, A.J.F. Kusumah, A. Lupitasari, D.N. Alfariza, R. Nuraini, et al., Recent trends of spinel ferrites (MFe_2O_4: Mn, Co, Ni, Cu, Zn) applications as an environmentally friendly catalyst in multicomponent reactions: a review, Case Studies in Chemical and Environmental Engineering 7 (2023) 100303.

[26] N. Garg, M. Basu, A.K. Ganguli, Nickel cobaltite nanostructures with enhanced supercapacitance activity, J. Phys. Chem. C 118 (31) (2014) 17332–17341.

[27] N. Girija, S.S. Kuttan, T. Anusree, B.N. Nair, A.A.P. Mohamed, U.N.S. Hareesh, Nickel foam-supported $NiCo_2O_4$ urchin-shaped microparticles sheathed with $NiCoO_2$ nanosheets as electrolyte-wettable electrodes for supercapacitors, ACS Applied Nano Materials 5 (10) (2022) 14529–14539.

[28] W. Luo, X. Wang, J. Li, Y. Wang, Y. Zhang, F. Meng, Study on morphology regulation and properties of $NiCo_2O_4@Co_3O_4$ nanocomposites: a facile strategy to obtain high-performance electrode materials, Colloids Surf. A Physicochem. Eng. Asp. 670 (2023) 131560.

[29] A. Ghadage, P. Kodam, D. Nadargi, K. Shinde, I. Mulla, J. Park, et al., Sponge microflowers of $NiCo_2O_4$: a versatile material for high performance supercapacitor, J. Porous. Mater. 29 (4) (2022) 1239–1252.

[30] A. Yan, W. Wang, B. Wang, X. Wang, J. Cheng, Core-shell structured $Co_3O_4@$ $NiCo_2O_4$ nanowires on nickel foam for supercapacitors, J. Electroanal. Chem. 907 (2022) 116061.

[31] N. Varalakshmi, A.L. Narayana, O. Hussain, N. Sreedhar, Improved supercapacitive performance of low pore size and highly stable nanostructured $NiCo_2O_4$ electrodes, J. Solid State Electrochem. 25 (2021) 1411–1420.

[32] N. Padmanathan, S. Selladurai, Controlled growth of spinel $NiCo_2O_4$ nanostructures on carbon cloth as a superior electrode for supercapacitors, RSC Adv. 4 (16) (2014) 8341–8349.

[33] P.-S. Hung, W.-A. Chung, S.-C. Chou, K.-C. Tso, C.-K. Chang, G.-R. Wang, et al., Composite $NiCoO_2/NiCo_2O_4$ inverse opals for the oxygen evolution reaction in an alkaline electrolyte, Cat. Sci. Technol. 10 (22) (2020) 7566–7580.

[34] S. Patil, N.D. Thorat, J. Bauer, S.A. Tofail, Metal oxide-based nanocomposites for supercapacitor applications, in: Advances in Metal Oxides and Their Composites for Emerging Applications, Elsevier, 2022, pp. 187–211.

[35] N. Wang, B. Sun, P. Zhao, M. Yao, W. Hu, S. Komarneni, Electrodeposition preparation of $NiCo_2O_4$ mesoporous film on ultrafine nickel wire for flexible asymmetric supercapacitors, Chem. Eng. J. 345 (2018) 31–38.

[36] C. Ji, F. Liu, L. Xu, S. Yang, Urchin-like $NiCo_2O_4$ hollow microspheres and $FeSe_2$ micro-snowflakes for flexible solid-state asymmetric supercapacitors, J. Mater. Chem. A 5 (11) (2017) 5568–5576.

[37] T. Ramachandran, F. Hamed, R.K. Raji, S.M. Majhi, D. Barik, Y.A. Kumar, et al., Enhancing asymmetric supercapacitor performance with $NiCo_2O_4$–NiO hybrid electrode fabrication, J. Phys. Chem. Solid 180 (2023) 111467.

[38] B. Junejo, Q.A. Solangi, A.S.B. Thani, I.M. Palabiyik, T. Ghumro, N. Bano, et al., Physical properties and pharmacological applications of Co_3O_4, CuO, NiO and ZnO nanoparticles, World J. Microbiol. Biotechnol. 39 (8) (2023) 220.

[39] A. Shah, A. Saleem, N.U. Amin, M. Salman, Y. Ling, A. Khesro, et al., Electrocatalytic performance investigation of $NiCo_2O_4$ nanostructures prepared by hydrothermal method and thermal post-annealing treatment, Mater. Sci. Eng. B 294 (2023) 116508.

[40] N.I.T. Ramli, A.M.M. Ali, N.H. Hussin, M.F. Mohamad Taib, O.H. Hassan, Unravelling the supercapacitive potential of Zn-Ni-Co mixed transition metal oxide, Recent Innovations in Chemical Engineering (Formerly Recent Patents on Chemical Engineering) 16 (3) (2023) 199–208.

[41] Y. Tao, W. Jiang, H. Wang, W. Hao, Q. Bi, X. Liu, et al., Tuning electronic structure of hedgehog-like nickel cobaltite via molybdenum-doping for enhanced electrocatalytic oxygen evolution catalysis, J. Colloid Interface Sci. 657 (2024) 921–930.

[42] T. Babii, K. Jirátová, J. Balabánová, M. Koštejn, A. Michalcová, J. Maixner, et al., Performance of nickel-manganese and nickel-cobalt-manganese mixed oxide catalysts in ethanol total oxidation, Catal. Today 428 (2024) 114438.

[43] J. Luo, X. Wang, Y. Gu, S. Wang, Y. Li, T. Wang, et al., Hierarchical sheet-like W-doped $NiCo_2O_4$ spinel synthesized by high-valence oxyanion exchange strategy for highly efficient electrocatalytic oxygen evolution reaction, Chem. Eng. J. 472 (2023) 144839.

[44] K. Alsamhary, F. Ameen, M. Kha, Biosynthesis cobalt-doped nickel nanoparticles and their toxicity against disease, Microsc. Res. Tech. 87 (2) (2024) 272–278.

[45] T.-B. Nguyen, C.-W. Chen, W.-H. Chen, X.-T. Bui, S.S. Lam, C.-D. Dong, NiCo$_2$O$_4$-loaded sunflower husk-derived biochar as efficient peroxymonosulfate activator for tetracycline removal in water, Bioresour. Technol. 382 (2023) 129182.

[46] S.V. Sadavar, N.S. Padalkar, R.B. Shinde, A.S. Patil, U.M. Patil, V.V. Magdum, et al., Graphene oxide as an efficient hybridization matrix for exploring electrochemical activity of two-dimensional cobalt-chromium-layered double hydroxide-based nanohybrids, ACS Applied Energy Materials 5 (2) (2022) 2083–2095.

[47] A. Banti, M. Charalampakis, P. Pardalis, C. Prochaska, S. Sotiropoulos, V. Binas, Electrochemical studies of inkjet printed semi-transparent NiCo$_2$O$_4$/ITO supercapacitor electrodes, Catalysts 13 (7) (2023) 1110.

[48] X. Hu, E. Tian, B. Wang, X. Zhou, L. Qiao, S. Liu, et al., Redox kinetics promoted by flower-like La$_2$CoMnO$_6$@NiCo$_2$O$_4$ heterojunctions for high-performance supercapacitors, J. Alloys Compd. 171129 (2023).

[49] C. Sakthivel, A. Nivetha, G. Thiruppathi, P. Sundararaj, I. Prabha, Synthesis of a multi-functionalized NiCo$_2$O$_4$ spinel heterostructure via the hydrothermal route for high-performance photo-electrocatalytic, anti-bacterial and eco-toxicity applications, New J. Chem. 47 (2) (2023) 571–588.

[50] X. Ji, H. Liang, S. Hu, B. Yang, K. Xiao, G. Yu, Highly efficient decomplexation of chelated nickel and copper effluent through CuO–CeO$_2$–Co$_3$O$_4$ nanocatalyst loaded on ceramic membrane, Chemosphere 334 (2023) 138981.

[51] R.S. Reena, A. Aslinjensipriya, S.G. Infantiya, R. Ragu, M. Jose, S.J. Das, Deciphering the role of pristine and Ni ions substituted Co$_3$O$_4$ nanoparticles with altered structural, magnetic and dielectric traits towards elevated photosensing and photocatalytic activity, Int. J. Environ. Anal. Chem. 1-38 (2023).

[52] C. Fan, Z. Ying, W. Zhang, T. Ju, B. Li, NiCo$_2$O$_4$ grown on Co/C hybrid nanofiber film with excellent electrochemical performance for flexible supercapacitor electrodes, J. Mater. Sci. Mater. Electron. 29 (2018) 6909–6915.

[53] S. Chen, P. Gao, D. Zhang, L. Lin, L. Huang, Z. Li, et al., Flexible asymmetric supercapacitors based on NiCo$_2$O$_4$ in a neutral electrolyte achieving 2.4 V voltage window, J. Alloys Compd. 860 (2021) 158346.

[54] S.V. Sadavar, N.S. Padalkar, R.B. Shinde, A.S. Patil, U.M. Patil, V.V. Magdum, et al., Lattice engineering exfoliation-restacking route for 2D layered double hydroxide hybridized with 0D polyoxotungstate anions: cathode for hybrid asymmetric supercapacitors, Energy Storage Materials 48 (2022) 101–113.

[55] S. Sadavar, K.J. Wang, T. Kang, M. Hwang, G. Saeed, X. Yu, et al., Anion storage for hybrid supercapacitor, Materials Today Energy 37 (2023) 101388.

[56] U.V. Shembade, S.D. Dhas, S.R. Gurav, R.G. Sonkawade, S.B. Wategaonkar, S. R. Ghatage, et al., Acid substitutions for WO$_3$ nanostructures synthesis by the hydrothermal route and its effect on physio-chemical and electrochemical properties for supercapacitors, Journal of Energy Storage 72 (2023) 108432.

[57] N.S. Padalkar, S.V. Sadavar, R.B. Shinde, A.S. Patil, U.M. Patil, D.S. Dhawale, et al., Layer-by-layer nanohybrids of Ni-Cr-LDH intercalated with 0D polyoxotungstate for highly efficient hybrid supercapacitor, J. Colloid Interface Sci. 616 (2022) 548–559.

[58] K.W. Ahmed, S. Habibpour, Z. Chen, M. Fowler, Investigation of NiCoO$_x$ catalysts for anion exchange membrane water electrolysis: performance, durability, and efficiency analysis, Journal of Energy Storage 79 (2024) 110149.

[59] D.P. PS, A. Philip, A.R. Kumar, An investigation on the compositional effects of 3D graphite on the electrochemical performance of NiO-Co$_3$O$_4$ composite, Diamond Relat. Mater. 141 (2024) 110597.

[60] A.M. Ghadimi, S. Ghasemi, A. Omrani, F. Mousavi, Nickel cobalt LDH/graphene film on nickel-foam-supported ternary transition metal oxides for supercapacitor applications, Energy Fuel 37 (4) (2023) 3121–3133.

[61] J. Yang, H. Li, S. He, H. Du, K. Liu, C. Zhang, et al., Facile electrodeposition of NiCo$_2$O$_4$ nanosheets on porous carbonized wood for wood-derived asymmetric supercapacitors, Polymers 14 (13) (2022) 2521.

[62] H. Zhang, D. Xiao, Q. Li, Y. Ma, S. Yuan, L. Xie, et al., Porous NiCo$_2$O$_4$ nanowires supported on carbon cloth for flexible asymmetric supercapacitor with high energy density, J. Energy Chem. 27 (1) (2018) 195–202.

[63] M.H. El-Shafei, A.G. El-Deen, A. Abd El-Moneim, A. Hessein, Controlled-synthesis of hierarchical NiCo$_2$O$_4$ anchored on carbon nanofibers mat for free-standing and highly-performance supercapacitors, J. Mater. Sci. Mater. Electron. 32 (12) (2021) 15882–15897.

[64] J. Zhang, Y. Wang, C. Yu, T. Zhu, Y. Li, J. Cui, et al., Hierarchical NiCo$_2$O$_4$/MnO$_2$ core–shell nanosheets arrays for flexible asymmetric supercapacitor, J. Mater. Sci. 55 (2) (2020) 688–700.

[65] R. Packiaraj, P. Devendran, K. Venkatesh, K. Mahendraprabhu, N. Nallamuthu, Unveiling the structural, charge density distribution and supercapacitor performance of NiCo$_2$O$_4$ nano flowers for asymmetric device fabrication, Journal of Energy Storage 34 (2021) 102029.

[66] B.H. Krishna, C.P. Reddy, P.R. Prasad, K. Mallikarjuna, I.N. Reddy, C. Bai, Copper cobalt oxide microstructures resembling marigold flowers were created by solvothermal synthesis for high-performance supercapacitors, Inorg. Chem. Commun. 160 (2024) 111922.

[67] M. Yewale, R. Kadam, U.T. Nakate, A. Teli, V. Kumar, S. Beknalkar, et al., Sphere-shaped CuCo$_2$O$_4$ nanostructures battery type electrode for supercapacitor via hydrothermal synthesis approach, Colloids Surf. A Physicochem. Eng. Asp. 679 (2023) 132541.

[68] D. Liu, Y. Liu, X. Liu, C. Xu, J. Zhu, H. Chen, Growth of uniform CuCo$_2$O$_4$ porous nanosheets and nanowires for high-performance hybrid supercapacitors, Journal of Energy Storage 52 (2022) 105048.

[69] E. Bao, X. Ren, R. Wu, X. Liu, H. Chen, Y. Li, et al., Porous MgCo$_2$O$_4$ nanoflakes serve as electrode materials for hybrid supercapacitors with excellent performance, J. Colloid Interface Sci. 625 (2022) 925–935.

[70] H. Chen, E. Bao, X. Du, X. Ren, X. Liu, Y. Li, et al., Advanced hybrid supercapacitors assembled with high-performance porous MnCo$_2$O$_{4.5}$ nanosheets as battery-type cathode materials, Colloids Surf. A Physicochem. Eng. Asp. 657 (2023) 130663.

[71] Y. Liu, X. Du, Y. Li, E. Bao, X. Ren, H. Chen, et al., Nanosheet-assembled porous MnCo$_2$O$_{4.5}$ microflowers as electrode material for hybrid supercapacitors and lithium-ion batteries, J. Colloid Interface Sci. 627 (2022) 815–826.

[72] X. Ren, E. Bao, X. Liu, Y. Xiang, C. Xu, H. Chen, Advanced hybrid supercapacitors assembled with beta-Co(OH)$_2$ microflowers and microclews as high-performance cathode materials, Colloids Surf. A Physicochem. Eng. Asp. 667 (2023) 131391.

[73] H. Shen, H. Li, M. Li, C. Li, L. Qian, L. Su, et al., High-performance aqueous symmetric supercapacitor based on polyaniline/vertical graphene/Ti multilayer electrodes, Electrochim. Acta 283 (2018) 410–418.

[74] S. Thareja, A. Kumar, High electrochemical performance of 2.5 V aqueous symmetric supercapacitor based on nitrogen-doped reduced graphene oxide, Energy Technology 8 (5) (2020) 1901339.

[75] Q. Xie, R. Bao, A. Zheng, Y. Zhang, S. Wu, C. Xie, et al., Sustainable low-cost green electrodes with high volumetric capacitance for aqueous symmetric supercapacitors with high energy density, ACS Sustain. Chem. Eng. 4 (3) (2016) 1422–1430.

[76] Y. Zhou, Z. Zhu, C. Zhao, K. Zhang, B. Wang, C. Zhao, et al., Reclaimed carbon fiber-based 2.4 V aqueous symmetric supercapacitors, ACS Sustainable Chemistry & Engineering 7 (5) (2019) 5095–5102.

[77] C. Li, W. Wu, P. Wang, W. Zhou, J. Wang, Y. Chen, et al., Fabricating an aqueous symmetric supercapacitor with a stable high working voltage of 2 V by using an alkaline–acidic electrolyte, Adv. Sci. 6 (1) (2019) 1801665.